Computational Discovery of Codoped Single-Atom

Catalysts for Methane-to-Methanol Conversion

Haojun Jia^{1,2}, Chenru Duan^{1,2}, Ilia Kevlishvili¹, Aditya Nandy^{1,2}, Mingjie Liu¹, and Heather J. Kulik^{1,2,*}

¹Department of Chemical Engineering, Massachusetts Institute of Technology, Cambridge, MA
02139, USA

²Department of Chemistry, Massachusetts Institute of Technology, Cambridge, MA 02139, USA

*Corresponding author email: hjkulik@mit.edu

ABSTRACT: The absence of a synthetic catalyst that can selectively oxidize methane to methanol motivates extensive study of single-site catalysts that possess a high degree of tunability in their coordination environments and share similarities with natural enzymes that can catalyze this reaction. Single-atom catalysts (SACs), and in particular doped graphitic SACs, have emerged as a promising family of materials due to their high atom economy and scalability, but SACs have yet to be exhaustively screened for methane-to-methanol conversion. Modulating the coordination environment near single metal sites by means of codopants, we carry out a large-scale highthroughput virtual screen of 2,048 transition metal (i.e., Mn, Fe, Co, and Ru) SACs codoped with various elements (i.e, N, O, P and S) in numerous spin and oxidation (i.e., M(II)/M(III)) states for the challenging conversion of methane to methanol. We identify that ground state preference is metal- and oxidation-state dependent. We observe a weak negative correlation between the oxo formation energy ($\Delta E(oxo)$) and the energy of hydrogen atom transfer ($\Delta E(HAT)$) thanks to the high variation of the coordination environment. Therefore, codoped SACs demonstrate flexible tunability that disrupts linear free energy relationships in a similar manner to homogeneous catalysts without losing the high scalability of heterogeneous catalysts. We identify energetically favorable catalyst candidates along the Pareto frontier of $\Delta E(oxo)$ and $\Delta E(HAT)$. Further kinetic analysis reveals an intermediate-spin Fe(II) SAC and a low-spin Ru(II) SAC as promising candidates that merit further experimental exploration.

KEYWORDS: methane-to-methanol conversion, single atom catalyst, computational catalyst design, density functional theory, codopant, high-throughput virtual screening

1. Introduction.

Methane, the second-most prominent greenhouse gas (GHG), contributes to approximately 16–20% of global GHG emissions¹. Converting methane to valuable chemicals (e.g., methanol) is seen as a key strategy to reduce methane emissions and therefore has great environmental significance and potential economic value. However, the direct conversion of methane to methanol is particularly challenging due to the high energy required to activate the strong C–H bonds of methane, which requires an efficient catalyst to lower the energy barrier, together with the thermodynamic favorability of methanol overoxidation to CO2^{2, 3}. The optimal catalysts for methane-to-methanol conversion need to satisfy numerous criteria, driving an exhaustive search of catalytic materials^{4, 5}. Enzymes (e.g., Fe(II) active sites in TauD⁶⁻⁸) have demonstrated the capability to selectively oxidize substrates with strong C–H bonds and motivated bioinspired design⁹⁻¹¹ of synthetic systems, including both homogeneous ¹²⁻¹⁷ and heterogeneous ¹⁸⁻²⁰ catalysts, for direct methane-to-methanol conversion. Although there has been substantial progress, no synthetic catalyst can simultaneously achieve as high activity and selectivity as enzymes, motivating a more extensive search for alternative catalysts.

Single-atom catalysts²¹⁻²⁸ (SACs), with isolated metal atoms dispersed on solid supports, have recently emerged as a captivating frontier, attracting intense research attention, although only limited study of SACs for direct methane-to-methanol conversion²⁹⁻³³ has so far been reported. SACs have the promise to combine the scalability of heterogeneous catalysts and the high atom economy of homogeneous catalysts^{34, 35}, offering significant opportunities for atom-economical utilization of metals³⁶⁻³⁸. Their unique electronic structure and unsaturated coordination environments have led to enhanced catalytic activity across numerous reactions^{39, 40} but also show great potential for energy storage and conversion^{41, 42}. Among different classes of SACs, N-doped

graphene SACs^{25, 28, 43}, featuring an isolated metal atom embedded in a graphitic material, more closely resemble their homogeneous counterparts compared to others. For instance, the Fe–N₄ active site in Fe-SACs are viewed as analogous to hemes^{40, 44-46}, where the Fe center is also coordinated to four nitrogen atoms, and molecular analogues have been developed to these SACs⁴⁷.

Although SACs exhibit attractive properties for catalysis, unraveling the catalytic mechanisms of SACs through experimental means faces significant challenges. The synthesis of SACs under harsh pyrolysis conditions results in a distribution of active sites^{43, 48-51} and significant variation of the local coordination environment^{50, 52, 53}, posing fundamental challenges for most characterization techniques, even for the highest-resolution spectroscopic techniques^{54, 55}. Similar to biological enzymes or transition metal complexes (TMCs), the spin state and oxidation state significantly influence the reactivity of SACs^{56, 57}, making it challenging to assess reactivity trends due to the difficulty of experiments that precisely identify the oxidation/spin states during catalysis^{39, 58}. To overcome these limits, first-principles modeling with density functional theory (DFT) has been a powerful tool for designing new SACs^{59,60} and obtaining mechanistic insights⁶¹-68 into their catalytic activities 69-74 with atomic precision. These DFT simulations 66, 67 have revealed that both the support and coordination environment of SACs are essential in determining their catalytic reactivity, consistent with the conclusions drawn from experimental characterization^{48, 52}. Thus, gaining a comprehensive understanding of the correlation between the structure and catalytic performance holds the key to achieving the rational design of SACs for targeted reactions at the atomic scale. Additionally, high-throughput virtual screening (HTVS)⁵⁶, 75-79 facilitates evaluation of an extensive library of catalyst candidates and the identification of promising ones. These approaches can be leveraged to elucidate the structure-reactivity relationships^{59, 60} of SACs and to investigate the role of structural change in catalytic reactions.

SACs with open-shell metal centers resemble single-site homogeneous and biological catalysts capable of catalyzing reactions such as C-H activation. The wide range of coordination configurations, enabled by various choices of the type and heterogeneity of coordination elements (i.e., N, O, P, and S), further allows for tuning the design and hence the structure-property relationship of SACs. Our previous work²⁸ investigated the rigid graphitic environment of SACs with N, O, P, and S coordination environments and compared them to homogeneous analogues for methane-to-methanol conversion, finding that differences in dopant sizes had major impacts on the structure and energetic properties of SACs. Further manipulation of the coordination sphere around the metal atom is paramount to unlocking the full potential of SACs and tailoring their catalytic activity and selectivity by fine-tuning the electronic structure and reactivity of the metal center, thus enhancing the catalytic performance^{51, 52}. Therefore, engineering the coordination environment near single metal sites by means of codopants^{49, 51-53, 57, 80} would be a way to design efficient SACs with optimal electronic structure for catalytic applications. Several codoping studies (e.g., N/S codopants in the first coordination sphere^{51, 53}, N/P codopants in the first coordination sphere⁵², and N in first with P in the second coordination sphere configuration⁴⁹) have been reported experimentally and shown significant potential for the oxygen reduction reaction (ORR), but the effect of codoping on methane-to-methanol conversion has not yet been reported.

In this work, we employ a HTVS approach to explore 2,048 transition metal (i.e., Mn, Fe, Co, and Ru) SACs codoped with various elements (i.e., N, O, P, and S) for the challenging conversion of methane to methanol. Initially, we investigate the global trends in spin state ordering and catalytic reaction energetics of the whole methane-to-methanol reaction cycle. Next, we focus on relationships between metal or codopant identity and reaction energetics, considering period dependence and coordination effects through the comparison of 3d and 4d codoped SACs (e.g., Fe

and Ru). In particular, best-trade-off catalyst candidates are identified along the $\Delta E(oxo)$ and $\Delta E(HAT)$ reaction energetics Pareto frontier. Finally, comprehensive characterization of the complete kinetic reaction coordinate validates the best-performing codoped SACs.

2. Model Systems

We modeled SACs with various metal-coordinating atoms (i.e., N, O, P, and S) in vacancies formed in 5- and 6-membered rings (Figure 1). Our previous²⁸ work indicates that dopants (i.e., N, O, P, and S) can module the local distortion around the metal site, which further allows for tuning the catalytic activity. The sizes of the 5- and 6-membered ring graphitic SAC systems investigated in this work are 59 and 61 atoms, respectively. Previous studies²⁸ have shown that even though finite-size effects of SAC flake models are not negligible, the qualitative trends and comparison of dopant-dependent SAC properties will hold and DFT modeling of finite-size SACs permits the use of accurate (i.e., hybrid) DFT functionals that are cost-prohibitive when using periodic boundary conditions. Moreover, we evaluate the effect of model size on oxo formation energy of representative SACs, which confirmed that the trends in dopant-specific energetics are preserved (Supporting Information Figure S1). To generate an expanded chemical space of SACs that are likely to be synthetically accessible by codoping the first and second coordination spheres, we define the local coordination environment of a SAC using three criteria: 1) the metal center; 2) the first coordination sphere atom identities (i.e., up to two dopant atom identities); 3) the second coordination sphere, which can contain dopants that are located in the smallest possible ring that contains all four metal-coordinating atoms (Figure 1).

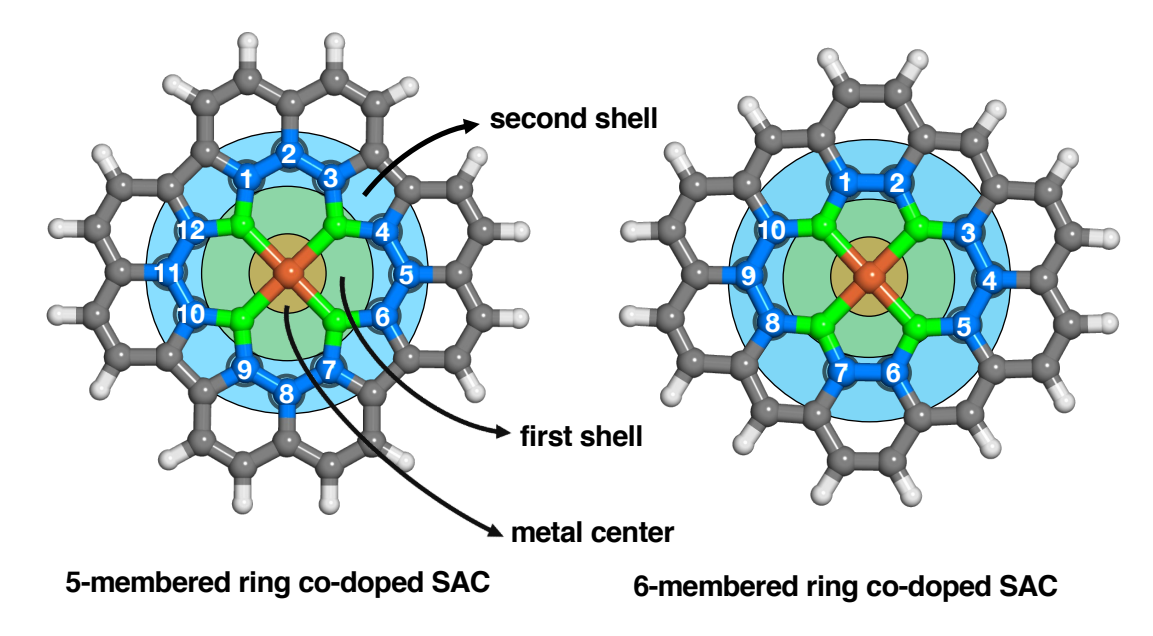


Figure 1. Schematic of the first and second coodination shells in the equatorial plane of 5- and 6-membered ring SACs. Regions of the SACs used to classify the local coordination environment are designated as metal center in orange, first coordination sphere in green and second coordination sphere in light blue. Numbers are used as labels for the position of dopants in the second coordination sphere. There are twelve and ten possible dopant positions in the second coordination sphere for 5- and 6-membered ring SACs, respectively. The structures are shown in the ball-and-stick representation and colored as follows: metal (Mn, Fe, Co, and Ru) in orange, C in gray, and H in white.

We investigate two distinct codoped SACs configurations: codoping only in the first coordination sphere or also codoping the second coordination sphere (e.g., atoms directly connected to the first coordination sphere). For any given dopant configuration, we used up to two distinct atoms. First, we codoped the first coordination sphere without doping any atoms in the second coordination sphere. This results in four distinct positional dopant configurations for each of the 6 atom combinations (e.g., NO, NP, NS, OS, OP, PS) for each 5- and 6-membered ring SAC, resulting in 48 total arrangements (Supporting Information Figures S2 and S3). The naming scheme for codoping in the first coordination sphere is ring size (e.g., 6-membered), metal and oxidation state (e.g., Fe(II)), and the identity and number of the dopants in the first coordination sphere (e.g., N₂O₂) along with any designation of symmetry (e.g., cis or trans) for the dopants

where relevant (e.g., 6-membered Fe(II)(trans N₂O₂)). In the 6-membered ring SAC, the four dopants in the first coordination sphere of 6-membered rings is not symmetric (e.g., NOON and NNOO are inequivalent), but these modestly inequivalent variations were ignored due to their limited effect on energetics (Supporting Information Table S1). For the second approach, we fixed the first coordination sphere to contain four N atoms, and codoped the second coordination sphere with two atoms that have the same identity (i.e., 2 N atoms, 2 O atoms, 2 P atoms, or 2 S atoms), following the doping reported in the experimental literature that tends to favor up to two unique elements and typically around two additional codopants in the second coordination sphere^{49, 81}. The naming scheme for codoping in both the first and second coordination spheres is ring size (e.g., 6-membered), metal and oxidation state (e.g., Fe(II)), positions for dopant in the second coordination sphere (e.g., 6 and 13 to make 6-13, see Figure 1), and the identity and number of the dopants in first (e.g., N₄) and second coordination sphere (e.g., S₂) for a configuration such as 6membered Ru(III)(6-13 N₄-S₂). We initially imposed an additional restriction that for atoms to be considered in the second sphere they had to be nearest neighbors to the first-coordination sphere dopants. We then expanded this definition, as motivated by experimental studies⁵⁷, to also include three types of bridging configurations (i.e., 5-membered Fe(II)(2-5 N₄-X₂), 5-membered Fe(II)(2-8 N₄-X₂), and 6-membered Fe(II)(4-9 N₄-X₂), where X is any co-dopant, see Supporting Information Figures S4 and S5). We repeated this for the 5- and 6-membered ring SAC models, resulting in 9 (11) distinct geometries for codoped 5-membered (6-membered) ring SAC models for a total of 80 arrangements (Supporting Information Figures S4 and S5).

In total, the 128 distinct codoped configurations combined with four metals in two oxidation states produces 2,048 transition-metal SACs in up to two spin states. After data filtering, our final codoped SAC dataset consists of over 700 catalysts (see Computational Details). From

this dataset, we identify strategies to engineer dopant configuration types and metal identities to tune catalyst energetics and discover optimal catalysts that can simultaneously activate methane and release methanol.

3. Reaction Mechanism

We calculate the reaction energetics of methane-to-methanol conversion by codoped SACs with four metals (M = Mn, Fe, Co, and Ru) in two oxidation states (i.e., M(II)/M(III)) in their corresponding spin states (Supporting Information Table S2). As in prior work^{5, 28, 56}, we compute energetics for the radical rebound mechanism⁸² for methane-to-methanol conversion starting from the resting state structure (1). In this mechanism, we form a high-valent terminal M(IV/V)=oxo (2) via two-electron metal oxidation by nitrous oxide^{83, 84}, a common oxidant (Figure 2). The oxo formation energy, $\Delta E(oxo)$, is computed as

$$\Delta E(oxo) = E(2) - E(1) + E(N_2) - E(N_20)$$
 (1)

Upon oxo formation, the metal formal oxidation state changes from M(II/III) to M(IV/V). Since we compute reaction energetics, an alternative oxidant choice would rigidly shift absolute reaction energetics but not influence relative catalyst energetics.

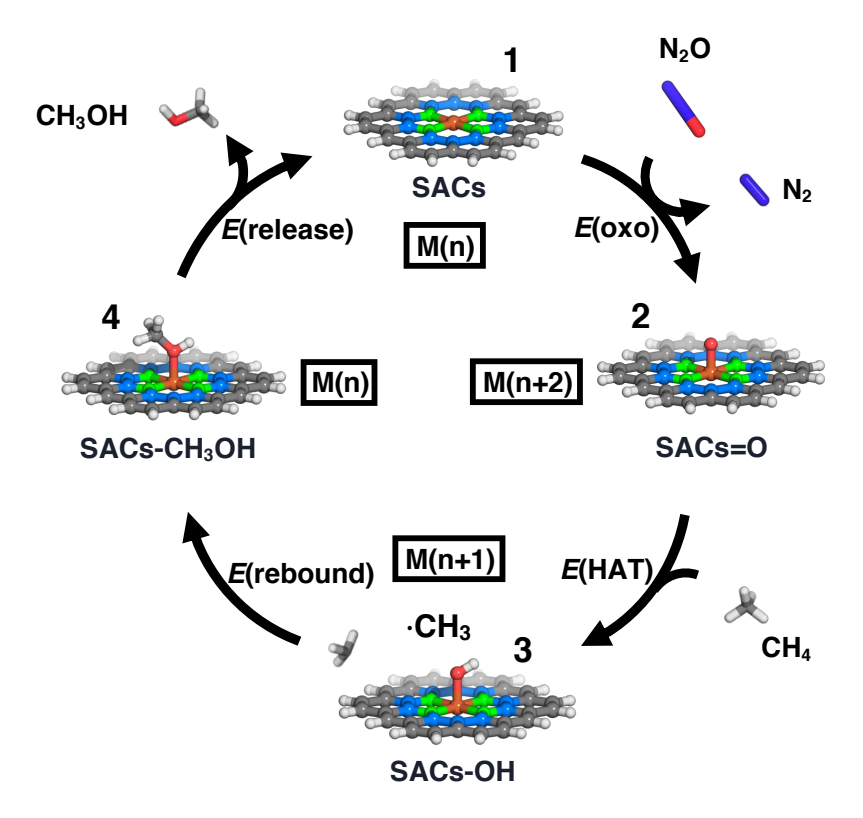


Figure 2. Catalytic cycle for the partial oxidation of methane to methanol. The catalytic cycle proceeds clockwise: from the resting state (1, top) in oxidation state n = II/III, metal—oxo (2, right) formation with an N₂O oxidant, followed by HAT to form a metal—hydroxyl complex (3, bottom), and rebound to form a methanol-bound intermediate (4, left). The structures are shown in the ball-and-stick representation colored as follows: metal center in orange, oxygen in red, nitrogen in dark blue, first coordination sphere dopant sites in green, second coordination sphere dopant sites in light blue, C in gray, and H in white.

After oxo formation, the high-valent M(IV/V)=O intermediate catalyzes hydrogen atom transfer (HAT) by abstracting a hydrogen atom from methane to form an M(III/IV)=OH intermediate (3) and a methyl radical (Figure 2). The reaction energy for the HAT step, $\Delta E(HAT)$, is calculated as:

$$\Delta E(HAT) = E(3) - E(2) + E(CH_3 \bullet) - E(CH_4)$$
 (2)

Following the HAT step, the recombination of the methyl radical with the M(III/IV)–OH intermediate in the radical rebound step forms a metal-bound methanol intermediate (4). We calculate the ΔE (rebound) energy as:

$$\Delta E(rebound) = E(4) - E(3) - E(CH_3 \bullet)$$
 (3)

To complete the catalytic cycle, CH_3OH is released from the catalyst to return it to the resting state (1). ΔE (release), is calculated as:

$$\Delta E(\text{release}) = E(\mathbf{1}) + E(CH_3OH) - E(\mathbf{4})$$
 (4)

All intermediates were investigated in low-spin (LS) states and intermediate-spin (IS) states for both the M(II/III) resting states and the M(IV/V)=O intermediates (see Computational Details).

4. Computational Details.

We performed all gas-phase geometry optimizations using density functional theory (DFT) with a development version of the GPU-accelerated electronic structure code TeraChem v1.9.85 We chose the range-separated hybrid functional $\omega PBEh^{86}$ (default $\omega = 0.2 \ bohr^{-1}$) to avoid the unphysical HOMO-LUMO gap closing that occurs in larger systems with global hybrid functionals. 87, 88 The LACVP* composite basis set was employed throughout our work, which consists of a LANL2DZ effective core potential^{89, 90} for metals and the 6-31G* basis for all other atoms. We confirmed that reaction energetics are not strongly sensitive to our omission of semiempirical dispersion, choice of functional (i.e., B3LYP global hybrid versus range-separated hybrid ωPBEh), and basis set size (i.e., def2-TZVP vs LACVP*, Supporting Information Figure S6). We carried out closed-shell singlet calculations in a spin-restricted formalism and all other calculations in a spin-unrestricted formalism that employed level shifting⁹¹ of 0.25 Ha for both majority- and minority-spin virtual orbitals to enable the convergence of the self-consistent field (SCF). We did not employ unrestricted calculations for singlets to avoid spin-contamination and did not employ restricted open shell calculations due to their slow convergence and higher computational cost that makes them prohibitive for high-throughput screening, thus we expect these singlets to be higher in energy than potential alternate solutions. We used the default SCF convergence threshold of 3x10⁻⁵ hartree for the direct inversion of the iterative subspace (DIIS)

error. We carried out geometry optimizations in the translation-rotation-internal coordinate $(TRIC)^{92}$ optimizer, with default tolerances for the maximum gradient of 4.5×10^{-4} hartree/bohr and the energy difference between steps of 1×10^{-6} hartree.

We simulated SAC systems with four transition metals (i.e., Mn, Fe, Co, and Ru) in two resting state oxidation states (i.e., II and III). Therefore, the total charge of the overall systems could vary, depending on the metal oxidation state and coordination environment. Following the same approach as our previous work²⁸, we simulated N and P coordinating atoms with a net -1 (0) charge for 5-membered (6-membered) ring SAC models. In contrast to the charge of N and P coordinating atoms, we simulated both O and S coordinating atoms with 0 charge in models for both 5-membered and 6-membered ring SACs. When there are an odd number of O or S coordinating atoms in 6-membered rings, we treated the flake model with +1 charge to satisfy the octet rule (Supporting Information Table S3). When we have a second coordinating shell dopant (i.e., N, O, P and S), all substitutions are made without altering net charge. All the catalytic intermediates were examined in both low-spin (LS) and intermediate-spin (IS) configurations, with the spin states being determined based on those that are applicable to both the resting state M(II/III) and the oxidized M(IV/V)=O intermediate. Specifically, this corresponds to LS singlet/IS triplet for 3d² Mn(V)=O, LS doublet/IS quartet for 3d³ Mn(IV)=O/ Fe(V)=O or 3d⁵ Co(IV)=O or 4d³ Ru(V)=O, and LS singlet/IS triplet for 3d⁴ Fe(IV)=O/Co(V)=O or 4d⁴ Ru(IV)=O (Supporting Information Table S2).

For the oxo intermediate in methane-to-methanol catalysis generated at SAC active sites, initial geometries were constructed using molSimplify⁹³, which uses OpenBabel⁹⁴ as a backend. We first optimized the LS state oxo intermediate with the metal-oxo bond distance set to 1.65 Å. After optimizing the metal-oxo intermediate, we geometry optimized the corresponding resting

state SACs by removing the oxygen atom. Following the procedure developed in our previous work⁵⁶, we also generated the metal-hydroxo intermediate using the metal-oxo intermediate as a starting point by adding an H atom to the optimized metal-oxo intermediate (Supporting Information Figure S7). The methanol-bound intermediates were generated in a similar fashion by adding a methyl group to the optimized metal-hydroxo intermediates using an in-house Python script (Supporting Information Figure S7).²⁸ All IS SAC intermediates were optimized from the corresponding pre-optimized LS structures (Supporting Information Table S2).

All job submissions were automated by the job manager in molSimplify with a 72-hour wall time per run cutoff and a maximum of five resubmissions for each job. ⁹⁵ If one intermediate optimization was not successful, the following downstream intermediate optimizations were not carried out. Converged structures were removed from the data set following established protocols^{28,56} if: 1) the expectation value of the S^2 operator, $\langle S^2 \rangle$, deviated from its expected value of S(S+1) by > 1; 2) the Mulliken spin density on the metal and oxygen differed from the spin multiplicity by > 1 μ_B ; or 3) the oxo moiety inserted into metal-coordinating bonds or deviated from the initial structure by a root-mean-square deviation (RMSD) > 0.6 Å. After all of these checks, the total number of converged and successful codoped SACs was 720 (Supporting Information Table S4).

We used ORCA v5.0.1⁹⁶ to calculate the transition states (TSes) and barrier heights of our best-performing codoped SACs because TeraChem does not support analytical Hessians. The TSes and barrier heights for the oxo formation and HAT step were modeled with the climbing image nudged elastic band (CI-NEB) method and bond length scan, respectively, followed by partitioned rational-function optimization (P-RFO) to locate transition state structures starting from a computed Hessian. For the bond length scan of the HAT step, the distance between the hydroxyl

hydrogen and the methyl radical carbon was scanned from 2.0 to 1.0 Å in 0.1 Å decrements while fixing the distance between the metal-oxo oxygen and the methyl radical carbon atom and letting all other atoms relax. Then, the maxima obtained from NEB calculations and the bond length scan served as initial guesses for P-RFO calculations to locate the TS structures. TS identities were confirmed through frequency calculations (i.e., by the presence of a single imaginary frequency).

5. Results and Discussion

5a. Global trends in spin state ordering and reaction energetics

Identification of the ground spin state of catalytic intermediates in the radical rebound methane-to-methanol catalytic cycle provides insight into reactivity trends and determines whether the process is spin-allowed or spin-forbidden. We first evaluate the broad trends of spin splitting energies, $\Delta E_{I-L} = E(IS)-E(LS)$, for the resting state, metal-oxo, metal-hydroxo, and methanolbound intermediates of codoped Mn, Fe, Co and Ru SACs (Figure 3). The ground state of codoped SACs varies significantly depending on the nature of the (co)dopants but is most sensitive to the metal and oxidation state. The resting state SAC structures for some metal/oxidation state combinations, Mn(II/III), Fe(II), Co(III) and Ru(II), have an IS ground state, whereas Fe(III), Co(II) and Ru(III) SACs have ground spin states that depend on the codopant configuration. For Fe(II) codoped SACs, all four reaction intermediates mostly have IS ground states (Figure 3). For the codoped SACs with most other metals, e.g., Mn(II/III), Fe(III), and Co(III), we find that most catalytic intermediates also have IS ground states although there are numerous exceptions (Supporting Information Figures S8–S11). However, there is no consistent typical ground spin state for all intermediates in SACs with Co(II) and Ru(II/III) metal centers (Supporting Information Figures S12–S14). For Mn(IV)=O, Ru(III)-OH, Ru(IV)-OH, Ru(III)-methanol SACs

intermediates, the LS is predominantly the ground state (Supporting Information Figures S8, S13, and S14). Thus, codoped SAC structures are likely to exist in both IS and LS states, potentially requiring spin-crossover for the most favorable catalyst energetics in Ru or Co(II), but IS states are the most likely ground states across the entire catalytic cycle for Mn(III) and Fe(II) codoped SACs.

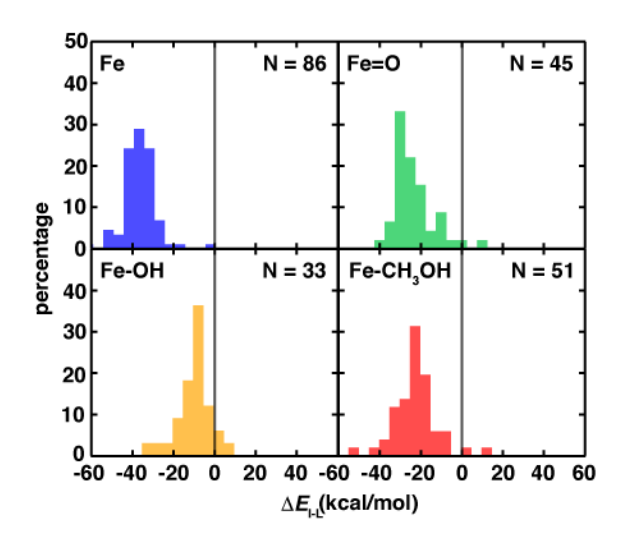


Figure 3. Histograms (bin width: 20 kcal/mol) of spin-splitting energies ($\Delta E_{I-L} = E(IS)-E(LS)$) for the resting state in blue (Fe, top left), metal—oxo in green (Fe=O, top right), metal—hydroxyl complex in orange (Fe-OH, bottom left), and methanol-bound intermediate in red (Fe-CH₃OH, bottom right) of Fe(II) codoped SACs. The total number of species used to compute each histogram is indicated in the top right corner of each panel. Zero axes are shown on all plots as solid black lines, with compounds on the left of the line favoring IS states and those on the right of the line favoring LS states.

We next investigated the trends in $\Delta E(oxo)$ and $\Delta E(HAT)$ reaction energetics across the codoped SACs data set in both LS and IS states. Over the codoped SACs set, we obtain a wide range of $\Delta E(oxo)$ (ca. 140 kcal/mol) reaction energies (Figure 4 and Supporting Information Figure S15). We observe distinct reaction energetics depending on the metal identity, oxidation state, and spin state, with LS Mn(II), IS Mn(II) and LS Fe(II) SACs most favorably forming metal-oxo species. Conversely, LS Co(II) SACs exclusively disfavor forming oxo intermediates, which is in agreement with generalization of the oxo wall theory to these square pyramidal coordination

geometries⁹⁷. However, there is no conclusive trend in $\Delta E(oxo)$ favorability for IS Fe(II) and IS Co(II) SACs. Over the same data set, $\Delta E(HAT)$ spans a narrower range (ca. 100 kcal/mol) than $\Delta E(oxo)$ and shows reduced metal dependence. The most energetically favorable candidates for $\Delta E(HAT)$ are LS Fe(II) and IS Co(II) codoped SACs, while the $\Delta E(HAT)$ reaction energetics are not typically favorable (i.e., $\Delta E > 0$) for other metal and spin states (Figure 4). We thus find LS Fe(II) codoped SACs are ideal candidates for direct methane-to-methanol conversion because LS Fe(II) codoped SACs have more favorable $\Delta E(HAT)$ (i.e., around 25 kcal/mol) while the $\Delta E(oxo)$ reaction energy is similar to IS Fe(II) codoped SACs. Nevertheless, although LS Fe(II) codoped SACs have favorable reaction energies, they are less likely to be the ground spin state for many intermediates during the reaction cycle. This observation underscores the challenges in discovering an optimal SAC for methane-to-methanol conversion.

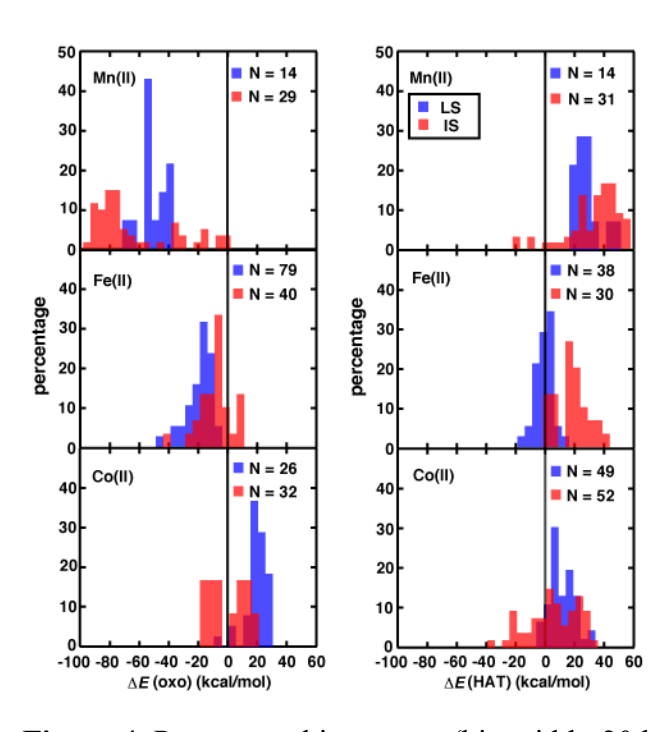


Figure 4. Percentage histograms (bin width: 20 kcal/mol) of $\Delta E(oxo)$ (left) and $\Delta E(HAT)$ (right) of codoped SACs grouped by metal (from top to bottom, Mn(II), Fe(II), and Co(II), colored by spin state (i.e., LS in blue and IS in red). The $\Delta E(HAT)$ values are for ferromagnetically coupled hydrogen atom transfer. The total number of intermediates used to compute each histogram is

indicated in the top right corner of each panel. The percentage is normalized separately for each spin state. Zero axes are shown on all plots as solid black lines.

Next, we evaluated the oxidation state (i.e., Fe(II) vs Fe(III)) influence on $\Delta E(oxo)$ and $\Delta E(HAT)$ reaction energetics for the codoped SACs (Supporting Information Figures S15 and S16). Here, we focus on investigating Fe-based SACs due to their favorable reaction energetics. Both the $\Delta E(oxo)$ and $\Delta E(HAT)$ of LS Fe(III) codoped SACs are less favorable than those of LS Fe(II), whereas the $\Delta E(oxo)$ and $\Delta E(HAT)$ energetics of IS Fe(II) and IS Fe(III) codoped SACs are similar. This observation is consistent with our prior study⁵⁶ suggesting the benefit of having a stronger Fe(III) oxidant is outweighed by more favorable $\Delta E(oxo)$ for Fe(II) without much penalty on $\Delta E(HAT)$ energetics relative to Fe(III). Our study here expands on that earlier observation to suggest that the benefit for HAT is indeed minimal for Fe(III) SACs.

Continuing through the reaction cycle to rebound, we observe that over the codoped SACs data set, ΔE (rebound) is predominantly favorable. The energetics nevertheless span a wide range from weakly (ca. 0 kcal/mol) to strongly (ca. -140 kcal/mol) exothermic (Supporting Information Figure S17). We observe near-zero rebound energetics for cases where N atoms codoped in the first and second coordination spheres, while several specific cases of SACs formed by M(III) metals with codopants in the first and second coordination spheres are strongly exothermic (i.e., -140 kcal/mol, Supporting Information Table S5). In general, the ΔE (rebound) values of codoped SACs show less metal dependence than ΔE (oxo) and ΔE (HAT). The ΔE (rebound) energetics of Mn, Fe and Ru codoped SACs show strong spin state dependency, with LS codoped SACs of these metals more near-zero energetics than that of their IS counterparts. Conversely, no strong spin state dependency is observed for Co codoped SACs. In terms of oxidation state dependence, we only observe significant dependence for Ru codoped SACs, which we attribute to the highly

diverse coordination environment and geometries in this study that make it difficult to isolate any specific effect of oxidation state (Supporting Information Figure S17).

In addition to oxo formation, HAT and rebound, the energetics of the release step could be unfavorable, leading to lack of conversion of methane to methanol by not allowing turnover or through overoxidation. Thus, we also compared broad trends in release energetics. We observe that all ΔE (release) energetics are unfavorable for the codoped SACs, with a wide range from weakly (ca. 2-3 kcal/mol) to strongly (ca. 90 kcal/mol) unfavorable values (Supporting Information Figure S18 and Table S6). The ΔE(release) energetics of codoped SACs vary significantly depending on the nature of dopants near the metal but are most sensitive to the metal identities. We observed the strongest penalty for releasing methanol for cases with only codopants in the first coordination sphere, whereas the interaction is weakened when SACs are also codoped in their second coordination sphere (i.e., 4 N in the first coordination sphere and 2 other dopants in the second coordination sphere, Supporting Information Table S6). The Δ E(release) values of Mn and Fe codoped SACs span a wide range (~ 10–90 kcal/mol), with strong oxidation and spin state dependence. In particular, we find ΔE (release) is more unfavorable for the higher oxidation state LS/IS Fe(III) and LS Mn(III) SACs, consistent with our previous observation on molecular catalysts⁵⁶, but the same trend is not observed for IS Mn(III) SACs (Supporting Information Figure S18). On the other hand, the distributions of ΔE (release) energetics of Co and Ru codoped SACs are much narrower, ranging from 10 to 40 kcal/mol. Perhaps due to this reduced variation, we also do not observe any oxidation- and spin-state-dependent trends for Co and Ru codoped SACs (Supporting Information Figure S18). In terms of optimizing SACs for release, Ru codoped SACs with more thermoneutral ΔE(release) values show promise as candidate catalysts for methane-tomethanol. In addition, we assess the methanol overoxidation in selected codoped SACs,

considering the energetic unfavorability of ΔE(release). Our observations indicate that E(SAC-OH + SAC-CH₂OH) could be more favorable than E(SAC=oxo + SAC-CH₃OH) suggesting that SACs with CH₃OH bound would overoxidize to SACs-CH₂OH in the presence of a closely spaced SAC=oxo (Supporting Information Table S7). However, doped graphitic SACs with well-isolated metal sites are highly dispersed on graphitic supports, which would effectively avoid this mechanism of methanol overoxidation in methane-to-methanol catalytic cycle. Overall, both Fe and Ru SACs appear to offer the best trade-offs for all reaction steps, whereas Co or Mn catalysts destabilize oxo or HAT intermediates, respectively.

5b. Period trends in codoped transition metal SACs

Although less earth abundant than 3d transition metals, 4d transition metals often form catalysts with superior catalytic performance (e.g., Ru for water oxidation^{98,99} or hydrogenation¹⁰⁰) compared to 3d transition metal catalysts. A compounding consideration is that according to hard-soft acid-base (HSAB) theory^{101, 102}, 4d metals should prefer to be coordinated by softer 3p ligands whereas 3d metals prefer 2p ligands. Thus, we need to investigate both metal and ligand period effects simultaneously to understand changes in catalytic activity.

To investigate the impact of 3d vs. 4d period trends (i.e., Fe(II) vs Ru(II)) on reaction energetics in codoped transition metal SACs, we focused on the $\Delta E(\text{oxo})$ and $\Delta E(\text{HAT})$ reaction step energetics of both LS and IS Fe(II) and Ru(II) codoped SACs. The $\Delta E(\text{oxo})$ and $\Delta E(\text{HAT})$ reaction energetics of LS Fe(II) are both better than IS Fe(II) SACs; $\Delta E(\text{HAT})$ energetics are more favorable for LS Ru(II) SACs than IS Ru(II) counterparts while $\Delta E(\text{oxo})$ values are comparable (Supporting Information Figure S19). Comparing the LS Fe(II) and Ru(II) codoped SACs, we observe that $\Delta E(\text{oxo})$ is less favorable (by ca. 10 kcal/mol) for LS Fe than for LS Ru. Conversely, $\Delta E(\text{HAT})$ is more favorable for LS Fe (by ca. 15 kcal/mol). For IS SACs counterparts, this trend

is even stronger, with $\Delta E(oxo)$ significantly less favorable in Fe codoped SACs than in Ru codoped SACs (by ca. 20 kcal/mol) while $\Delta E(HAT)$ is more favorable for Fe than in Ru codoped SACs (by ca. 20 kcal/mol). These energetic trends suggest that the combination of the confined active site with the more diffuse orbitals of the Ru center leads to more favorable formation of the oxidized metal-oxo, at the cost of worsened HAT performance. Nevertheless, individual catalysts can deviate significantly from this average trend, motivating our comparison of both Ru and Fe SAC catalytic cycles (see Sec. 5d).

In order to understand the period dependence and coordination environment effects (2p, a)combination of 2p and 3p, and 3p) on reaction energetics, we evaluate variations with dopant atoms for $\Delta E(oxo)$ and $\Delta E(HAT)$ of Fe and Ru codoped SACs with the same coordination environment (Figure 5). Overall, the 3p (i.e., P or S) dopants in codoped SACs make $\Delta E(HAT)$ more favorable but $\Delta E(oxo)$ less favorable relative to 2p elements (i.e., N or O) in codoped SACs (Supporting Information Figure S20). This trend holds for Ru or Fe but is subtler than the earlier observation that ΔE(oxo) energetics on Fe codoped SACs are less favorable than Ru codoped SACs while ΔE(HAT) energetics on Ru codoped SACs are less favorable than Fe SACs (Supporting Information Figure S20). For the outliers to these general observations, e.g., LS 6-membered Ru(III)(6-8 N₄-S₂) SACs versus LS 6-membered Fe(III)(6-8 N₄-S₂) SACs, we identify that the inclusion of S dopants in the second coordination sphere induces distinct graphene flake distortion for Fe vs. Ru (Figure 5). This distortion occurs in opposing directions between the LS 6-membered Ru(III)(6-8 N₄-S₂) SACs and the LS 6-membered Fe(III)(6-8 N₄-S₂) SACs. The trend in increasing HAT favorability for 3p dopants is similar to those that have been previously observed for Fe(II) complexes for methane-to-methanol conversion¹⁰³. Nevertheless, in other cases, the origin appears more electronic in nature, such as a 6-membered Fe(II)(N₁O₃) SAC where oxo formation is more

favorable for Fe(II) than Ru(II), despite a weaker ligand field (Figure 5). Overall, both electronic and structural differences in 2p and 3p dopants play a role in relative energetics of SAC catalysts, but the metal dependence (i.e., 3d vs 4d) is stronger than the dependence on coordination environment (i.e., 2p vs 3p).

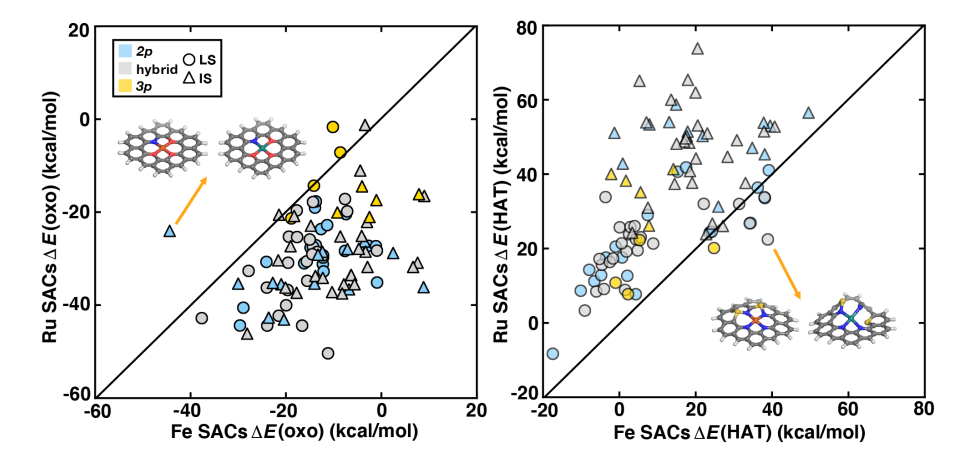


Figure 5. Parity plots of $\Delta E(oxo)$ (left) and $\Delta E(HAT)$ (right) reaction energies (in kcal/mol) between codoped Fe SACs and Ru SACs under the same flake and oxidation state conditions. Data are colored by coordination environment (2p in blue, a combination of 2p and 3p in gray and 3p in yellow) and distinguished by spin state (LS in circles and IS in triangles) as indicated in the legend. Two outliers of codoped SACs are shown in the parity plot: IS 6-membered Ru(II)(N₁O₃) SACs vs IS 6-membered Fe(II)(N₁O₃) SACs (left) and LS 6-membered Ru(III)(**6-8** N₄-S₂) SACs vs LS 6-membered Fe(III)(**6-8** N₄-S₂) SACs (right). Atoms are colored as follows: brown for Fe, dark teal for Ru, blue for N, red for O, yellow for S, gray for C, and white for H.

5c. Reaction energetics tradeoffs of codoped transition metal SACs

Often in HTVS for heterogeneous catalysts, linear free energy relationships (LFERs) are leveraged to correlate energetics of individual intermediates to the holistic catalytic activity^{70, 72}. The $\Delta E(\text{oxo})$ and $\Delta E(\text{HAT})$ reaction energies typically have a strong negative correlation (i.e., a negative slope LFER) for heterogeneous catalysts, while the LFER is known to be weak in homogeneous catalysts⁵⁶. In light of the extensive utilization of LFERs to simplify a complex catalytic cycle into a single representative descriptor, we aimed to determine whether a diverse

chemical space of codoped transition metal SACs follow established LFERs^{70, 104} for the radical rebound mechanism of direct methane-to-methanol conversion by comparing trends in the four metals (i.e., Mn, Fe, Co, and Ru, see Computational Details). Over our codoped SACs dataset, we observe a relatively weak global negative correlation between $\Delta E(oxo)$ and $\Delta E(HAT)$ (Figure 6, Supporting Information Figure S21). This lack of global correlation motivates determination of metal- and spin-state-dependent LFERs.

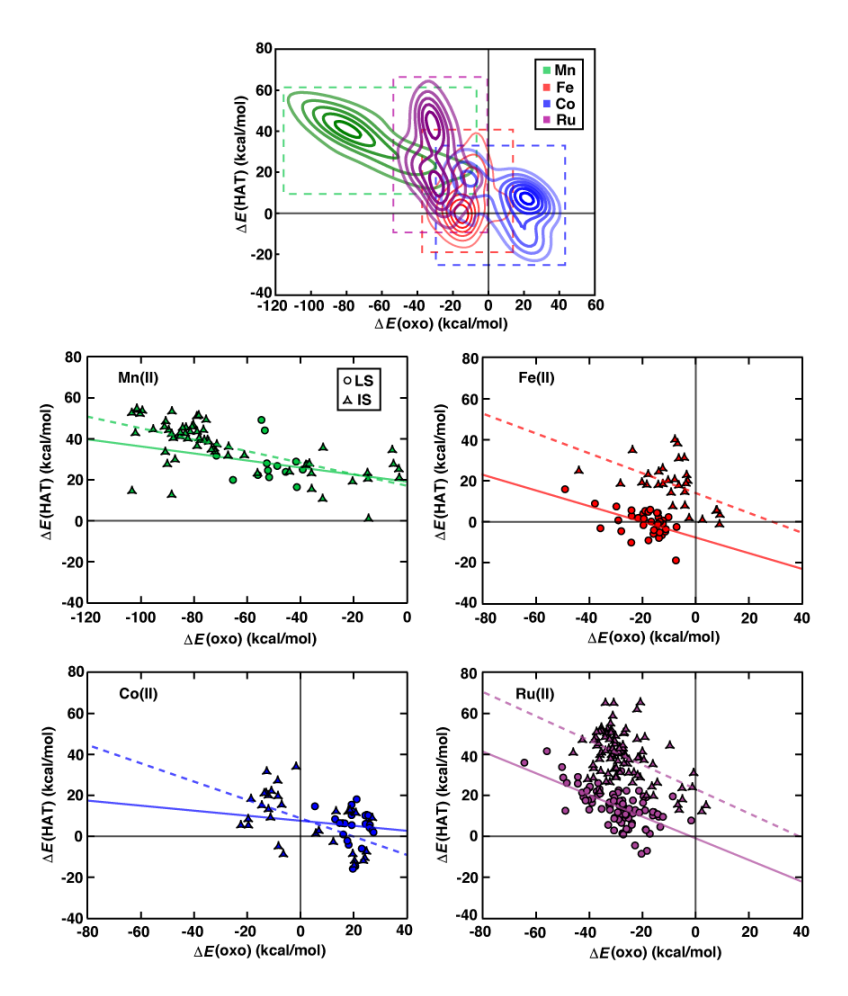


Figure 6. $\Delta E(oxo)$ vs. $\Delta E(HAT)$ reaction energies (in kcal/mol) of codoped M(II) SACs shown as metal-dependent Gaussian kernel density estimates (KDEs, top) and explicit data points for the Mn(II) (middle left), Fe(II) (middle, right), Co(II) (bottom, left), and Ru(II) (bottom, right) panes. The KDEs and explicit data points are colored by metal identities (Mn in green, Fe in red, Co in blue, and Ru in purple). The KDEs of the distributions for the codoped SACs are shown as contour lines with decreasing saturation in 10 evenly spaced levels. Dashed colored outlines in the KDEs correspond to the ranges of $\Delta E(oxo)$ and $\Delta E(HAT)$ of Mn, Fe, Co and Ru codoped SACs. Explicit data points are distinguished by spin state (LS in circles and IS in triangles) as indicated in the

legend. The solid lines are linear fits for the LS codoped SACs and dashed lines are equivalent fits for IS systems. Zero axes are shown on all plots as solid black lines.

Indeed, we observe the degree of correlation between the $\Delta E(oxo)$ and $\Delta E(HAT)$ reaction energetics to vary by metal and spin state. In particular, IS Mn(II) codoped SACs exhibit the strongest correlation between the two reaction energies among all codoped SACs (Pearson's r = -0.67, Figure 6 and Supporting Information Table S8). Notably, this correlation is accompanied by a shallow slope of -0.28, indicating that the formation of stable Mn-oxo SACs does not correspond to a significant reduction in favorability for HAT. Nevertheless, all IS Mn(II) codoped SACs have unfavorable $\Delta E(HAT)$ reaction energetics, with relatively high values in the range of 20–40 kcal/mol (Figure 6). In contrast, the LS Co(II) codoped SACs show among the weakest correlation between $\Delta E(oxo)$ and $\Delta E(HAT)$ reaction energetics (Pearson's r = -0.08) and relatively little tradeoff between the two steps (slope of -0.12, Figure 6 and Supporting Information Table S8). The observations on codoped SACs of weakened LFERs is consistent with our previous observations for transition metal complexes⁵⁶, including metal- and spin-specific trends such as the weak correlation for LS Co. We attribute the weak correlation between $\Delta E(oxo)$ and $\Delta E(HAT)$ in codoped SACs to the high variation of the coordination environment (i.e., both material composition and geometric configurations).

Beyond metal identity, SACs with different spin states show significantly different behavior in terms of the slope and intercept for a linear fit (Supporting Information Table S8). Among all metal and oxidation state combinations, those with a low-spin d^6 electron configuration, i.e., LS Fe(II) and LS Co(III), most likely form codoped SACs with both favorable (i.e., $\Delta E < 0$) oxo and HAT energetics thanks to a modest trade-off in the two reaction energies (Figure 6 and

Supporting Information Figure S21). Therefore, codoped SACs have flexible tunability that allows for disrupting LFERs as in homogeneous catalysts.

5d. Catalytic cycles of codoped SACs with the best energetic trade-offs

Despite weak LFERs, all SAC catalyst candidates have at least some trade-off in reaction energetics between multiple steps in the radical-rebound mechanism. Here, we first consider the trade-off of reaction energetics between $\Delta E(HAT)$ and $\Delta E(oxo)$, which are the potential ratelimiting steps in the catalytic cycle for methane-to-methanol conversion⁸². The best catalysts should have an optimal trade-off between $\Delta E(oxo)$ and $\Delta E(HAT)$ reaction energetics (i.e., not favoring one too strongly at the cost of disfavoring the other). We thus define a Pareto front consisting of the catalysts with the best trade-off between $\Delta E(oxo)$ and $\Delta E(HAT)$ reaction energies. Based on the Pareto frontier, we identify six total catalyst candidate SACs: four lying on the Pareto frontier of $\Delta E(oxo)$ and $\Delta E(HAT)$ (A: LS 5-membered Mn(III)(O₃P₁), B: LS 5membered Fe(II)(6-11 N₄-S₂), C: IS 6-membered Fe(II)(cis N₂O₂) and E: LS 6-membered Fe(II)(14-15 N₄-P₂)) and the two next closest catalysts to the Pareto frontier (D: LS 5-membered Ru(II)(14-16 N₄-N₂) and F: LS 6-membered Co(II)-(cis O₂P₂)), for direct methane-to-methanol conversion. Surprisingly, despite average trends indicating favorable formation of metal-oxos by Ru catalysts, the best Ru-based codoped SAC (i.e., **D**) does not reach the Pareto frontier spanned by the 3d transition metal SACs, reinforcing the greater potential of light, earth-abundant transition metal SACs for direct methane-to-methanol conversion (Figure 7). We find Fe(II)-based codoped SACs are most likely to be favorable (i.e., both $\Delta E(oxo)$ and $\Delta E(HAT) < 0$) compared to SACs with other metal centers. In comparison to A or F, which have extremely favorable reaction energetics for either $\Delta E(oxo)$ or $\Delta E(HAT)$ and unfavorable reaction energetics on the other, the Fe(II)-based codoped SACs along the Pareto front display more moderate tradeoffs. If Brønsted–Evans–Polanyi (BEP) relations^{73, 105} hold, one would ideally minimize ($\Delta E(oxo) + \Delta E(HAT)$) to achieve the optimal balance between $\Delta E(oxo)$ and $\Delta E(HAT)$ reaction energetics (Supporting Information Table S9). Based on this criterion, we can conclude that **A** and **C** provide an optimal trade-off between $\Delta E(oxo)$ and $\Delta E(HAT)$, which we quantitatively determine by computing the sum of $\Delta E(oxo)$ and $\Delta E(HAT)$ (Supporting Information Table S9). Importantly, **C** is spin-allowed in catalytic cycle of methane-to-methanol reaction (i.e., the resting state and all intermediates have the same ground-state spin) (Supporting Information Tables S10 and S11).

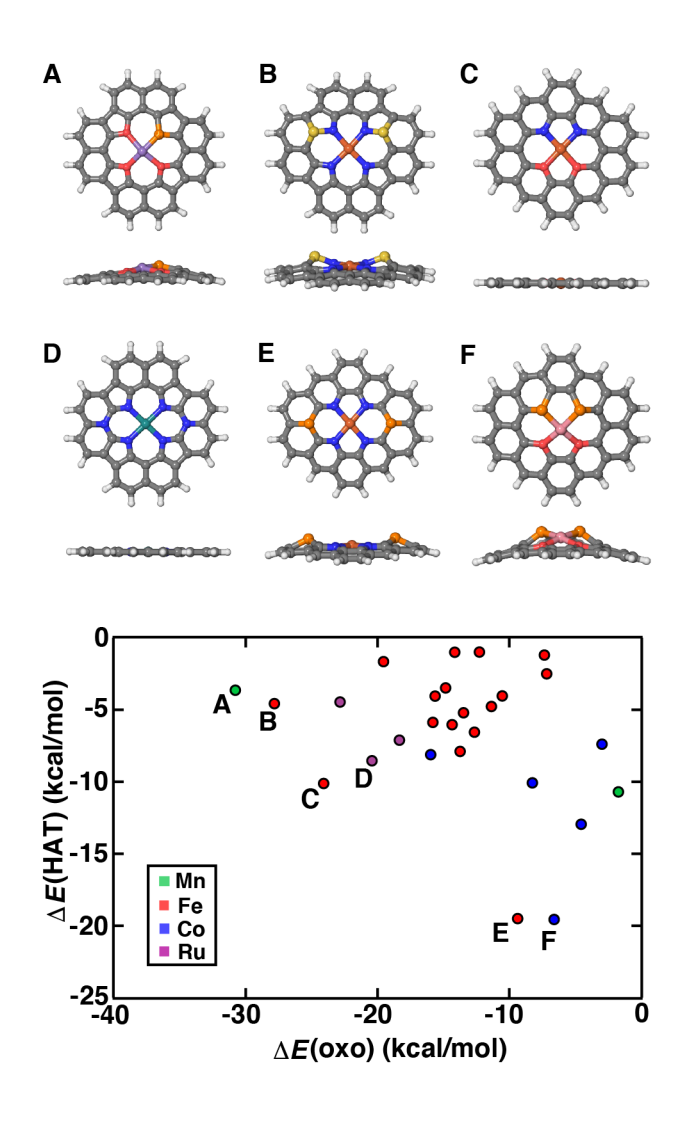


Figure 7. Examples of the best-trade-off catalysts (top) across codoped SACs dataset are indicated by letters A–F. The $\Delta E(oxo)$ vs. $\Delta E(HAT)$ reaction energies (in kcal/mol) of the best performing catalysts (bottom) are colored by metal identities (Mn in green, Fe in red, Co in blue, and Ru in

purple). Only SACs with both energetically favorable $\Delta E(oxo)$ and $\Delta E(HAT)$ reaction energetics are shown. On top (from left to right) are the codoped SACs from **A**: LS 5-membered Mn(III)(O₃P₁) SAC, **B**: LS 5-membered Fe(II)(**6-11** N₄-S₂) SAC, **C**: IS 6-membered Fe(II)(cis N₂O₂) SAC, **D**: LS 5-membered Ru(II)(**14-16** N₄-N₂) SAC, **E**: LS 6-membered Fe(II)(**14-15** N₄-P₂) SAC, and **F**: LS 6-membered Co(II)-(cis O₂P₂) SAC. Atoms are colored as follows: purple for Mn, brown for Fe, pink for Co, dark teal for Ru, blue for N, red for O, orange for P, yellow for S, gray for C, and white for H.

Next, we proceed to compare the catalytic performance of the Fe(II) SAC \mathbf{C} , which has two N and two O atoms codoped in the first coordination sphere, with the pure N-doped SAC models. The N-doped SACs from our previous study²⁸ have four N atoms coordinating in the first coordination sphere with 5- or 6-membered ring structures. These N-doped SACs have similar $\Delta E(\text{oxo})$ energetics (i.e., ca. -10 kcal/mol) along with favorable $\Delta E(\text{HAT})$ (i.e., -3.4 kcal/mol for 5-membered ring and -6.8 kcal/mol for 6-membered ring N-doped SACs). In comparison to the pure N-doped SACs in our previous study²⁸, we observe that introducing O dopants with N dopants in the first coordination sphere of SACs, as in the candidate \mathbf{C} , leads to significant improvements in both $\Delta E(\text{oxo})$ and $\Delta E(\text{HAT})$ reaction energetics (i.e., by > 5 kcal/mol). This observation can be ascribed to the electronic environment created by multiple dopants, which cannot be accessed by a single dopant element. On the basis of this analysis, employing N/O codopants in the first coordination sphere may provide an approach to improve catalytic performance of these materials for methane-to-methanol conversion.

To validate our best-trade-off codoped SACs designs, we now characterize the full reaction coordinate, i.e., with both transition states (TS) and reaction intermediates, of the selected codoped SACs for the radical rebound mechanism of methane-to-methanol conversion. Here, we focus our analysis on the codoped SACs: **A**, **C**, **D** and **E** after omitting **B** and **F** because we were unable to fully converge the pathway for oxo formation on these SACs with CI-NEB. Of these four

remaining catalysts, all have favorable reaction energetics, and \mathbf{C} is in its ground spin state. As the $\Delta E(oxo)$ and $\Delta E(HAT)$ steps play crucial roles as potential rate-limiting steps in the catalytic cycle of methane-to-methanol conversion, we calculate kinetics properties associated with oxo formation and HAT with NEB and potential energy scans, respectively (see Computational Details). The radical rebound step has been shown to be nearly barrierless and not involved in the turnover-determining transition state (TDTS) in our previous work⁵, and so we do not attempt to compute a barrier for it.

We observe comparatively low oxo formation barriers of 17.3 kcal/mol for C and 4.0 kcal/mol for **D**, indicating relatively facile formation of metal-oxo species for C–H bond activation in methane (Figure 8). In contrast, the oxo formation barriers of A and E are considerably higher (i.e., 31.3 kcal/mol and 26.7 kcal/mol, respectively), which is also noteworthy that both activation energies are relatively similarly high even though they were on the opposite ends of the Pareto front in terms of oxo formation energetic favorability (Figure 8). Among the four selected codoped SACs, the HAT barrier of ground state C exhibits the lowest HAT barrier energy at 14.7 kcal/mol, followed by **D** with a moderate barrier of 21.6 kcal/mol. Compared to the **C** and **D** systems, **E** has a higher HAT barrier energy of 39.0 kcal/mol indicating that it requires more energy for HAT and is unlikely to be a proficient catalyst for direct methane-to-methanol conversion. The A SAC has the highest HAT barrier energy at 44.5 kcal/mol, making it the most energetically demanding for the HAT process and unlikely to feasibly catalyze HAT, even when accounting for uncertainty due to error in the DFT functional (Supporting Information Table S12). Comparing these energetics, we observe at most a qualitative BEP relationship in the HAT step: the most favorable SAC in terms of reaction energetics, C, has the lowest kinetic barrier while the most unfavorable SAC, A, has the highest kinetic barrier. There are, however, exceptions for **D** and **E**, where the kinetic

barriers are drastically different although their energetics are similar (Supporting Information Figure S22). This observation, which we ascribe to the diverse chemistry of the metal, oxidation state, spin state, and coordination environment combinations we included in this study, highlights the importance of explicit evaluation of kinetic barriers in identifying favorable SACs. We also performed an analysis of the total density of states (DOS) but did not observe significant correlations between electronic structure and the energetics of catalytic reactions (Supporting Information Figure S23). For the methane-to-methanol conversion studied, codoped SACs were simulated assuming a radical rebound mechanism, meaning that the thermodynamic results of other potential mechanistic pathways, e.g., proton-coupled electron transfer (PCET), could vary.

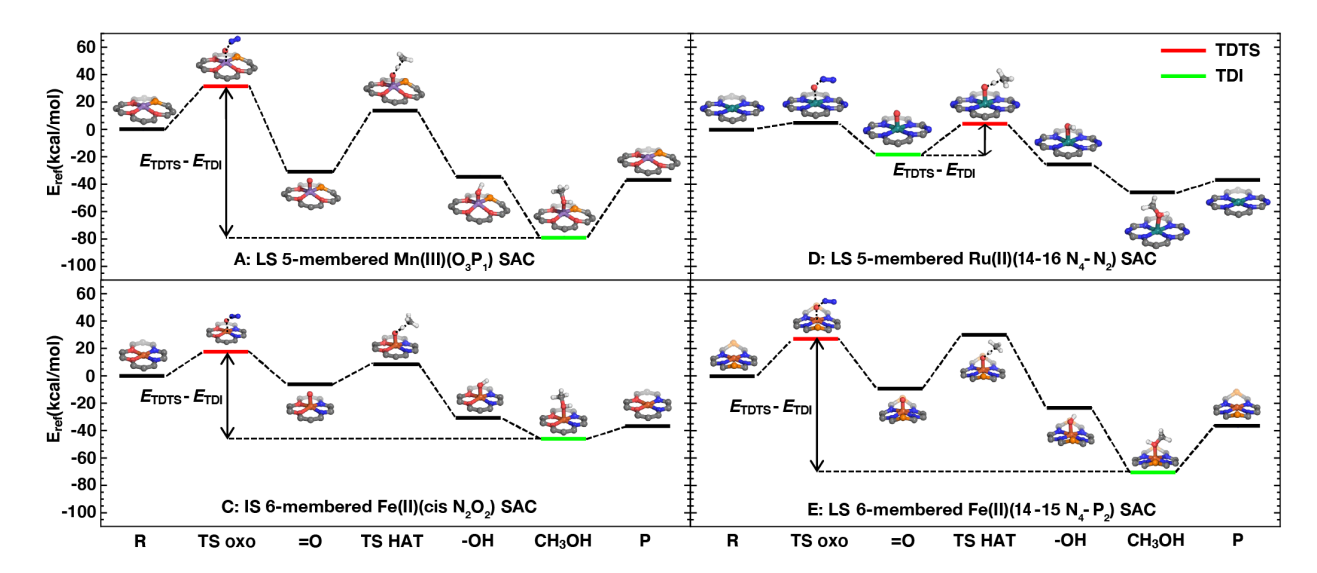


Figure 8. Full energy landscapes (E_{rel} in kcal/mol) of the four best-trade-off codoped SACs with **A**: LS 5-membered Mn(III)(O₃P₁) (top left), **C**: IS 6-membered Fe(II)(cis N₂O₂) (bottom left), **D**: LS 5-membered Ru(II)(**14-16** N₄-N₂) (top right), and **E**: LS 6-membered Fe(II)(**14-15** N₄-P₂) (bottom right). The reaction coordinates are labeled with intermediates: the reactants (R), the TS of oxo formation (TS oxo), the metal-oxo intermediate (=O), the TS of HAT (TS HAT), the metal hydroxyl intermediate (-OH), the methanol-bound intermediate (CH₃OH), and the product (P). The turnover-determining TS (TDTS) and turnover-determining intermediate (TDI) are shown inset along with the energy differences between the TDTS and TDI (E_{TDTS} - E_{TDI}) that governs efficiency of catalysis. The TDTS and TDI are labeled with red and green, respectively. Atoms are colored as follows: purple for Mn, brown for Fe, dark teal for Ru, blue for N, red for O, orange for P, gray for C, and white for H.

Next, we employed the energetic span model to estimate the catalytic turnover frequency (TOF) of the four selected codoped SACs. We observe that A, C and E share a common TDTS associated with the oxo formation step (Figure 8, Supporting Information Table S13). Additionally, the turnover-determining intermediate (TDI) for those three codoped SACs is the methanol-bound intermediate. However, as for **D**, the TDTS associated with the TS HAT and the TDI is the metal-oxo intermediate due to moderate methanol release energetics. The energetic span (δE) differs significantly among the four codoped SACs with a wide variation of 60 kcal/mol. This range extends from 21.6 kcal/mol in **D** (i.e., likely to catalyze C–H activation) to 73.3 kcal/mol in A (i.e., unlikely to catalyze C–H activation), resulting in a large 37 order of magnitude difference in the computed catalyst TOFs (Supporting Information Table S13). Interestingly, **D** was one catalyst that was not on the Pareto front, only close to it, but our kinetic analysis highlights its superior performance, emphasizing the limited predictive capabilities of a reaction-energetics-only screen in SACs. Full kinetic screening of candidates might therefore reveal even better SAC candidates that are not on the reaction energetics Pareto front. Furthermore, our investigation reveals that the relative energetics and energy spans associated with methane oxidation for our selected codoped SACs, C and D, are comparable to the computed energy spans reported in macrocyclic molecular complexes⁵ and metal-organic framework nodes^{84, 106, 107}. Given the favorable reaction energetics, kinetics, and TOF of C and D, we conclude that C and D are the most promising codoped SACs for methane-to-methanol conversion and merit further experimental exploration. While our computational predictions suggest promising catalytic characteristics for C and D, experimental validation of these candidates on their stability under reaction conditions will be necessary in future study.

6. Conclusions

Using a high-throughput virtual screening (HTVS) approach, we investigated 2,048 codoped transition metal (i.e., Mn, Fe, Co, and Ru) SACs in numerous spin and oxidation states for the challenging conversion of methane to methanol. Here, we focused on modulating the coordination environment by doping in both the first and second coordination spheres, to design efficient SACs and alter the catalytic properties for direct methane-to-methanol conversion. To determine the ground spin state of catalytic intermediates of SACs, we first explored the impact of the influence of metal/oxidation state in SACs. We found that SACs can have either IS or LS ground states in the catalytic cycle depending on the transition metal center. Next, we evaluated the relationship of the energetics of oxo formation and HAT steps in codoped transition metal SACs. Across our codoped SACs dataset, we observed a relatively weak negative correlation between $\Delta E(oxo)$ and $\Delta E(HAT)$. We attribute the weak correlation to the significant variation of the coordination environment among these SAC catalysts, especially the structural variation in the first coordination sphere. The ΔE (release) energetics are endothermic for the codoped SACs, with a wide-spread range for Fe and Mn codoped SACs but are quite narrow for Co and Ru codoped SACs. We expect the flexible tunability demonstrated here, which allows disruption of LFERs as in molecular catalysts, should combine with the stability and scalability of SAC catalysts in general to benefit from the advantages of both homogeneous and heterogeneous catalysts. In order to understand the periodic trends and coordination environment effects on reaction energetics, we compared Fe and Ru reaction energetics and found Ru formed more stable metal-oxos, while Fe HAT energetics were more favorable. Conversely, ΔE(HAT) energetics in LS Ru codoped SACs are less favorable than those in all LS Fe SACs, and most IS Ru systems exhibit far less favorability than IS Fe systems.

Finally, we considered the trade-off between $\Delta E(HAT)$ and $\Delta E(oxo)$ and identified catalyst

candidates along the $\Delta E(oxo)$ and $\Delta E(HAT)$ Pareto frontier through reaction energetics

assessments. Owing to weak BEP relations over this set, we found that points close to but not on

the Pareto frontier had superior kinetic properties. Our kinetic analysis on the best-trade-off subset

of SACs results recommended that the following two codoped SACs hold great promise for

methane-to-methanol conversion: C: IS 6-membered Fe(II)(cis N₂O₂) SAC and D: LS 5-

membered Ru(II)(14-16 N₄-N₂) SAC. Overall, our analysis of codoped SACs indicated the

performance of SAC active sites is strongly influenced by both first and second coordination

sphere element identities as well as by the local geometric structures they favor. By strategically

engineering the local coordination environment, not just in the first coordination sphere but also

the second, there are untapped opportunities to fine-tune the energetics of the HAT and oxo

formation steps that normally are expected to have a steep tradeoff. Among the codoped SACs

studied, we identify SAC candidates with promising reaction energetics, kinetics and turnover

frequencies for methane-to-methanol catalysis, warranting further experimental exploration.

AUTHOR INFORMATION

Corresponding Author

*email:hjkulik@mit.edu

Notes

The authors declare no competing financial interest.

ASSOCIATED CONTENT

Supporting Information. Energetics of increasingly large codoped SACs; Geometry configurations of codoped SACs; symmetry 6-membered ring SAC; spin state of codoped SACs; functional, basis-set and dispersion correction sensitivity of $\Delta E(oxo)$; charge of codoped SACs;

30

workflow for generating reaction energetics; attrition of calculations; statistics and histograms of spin-splitting energies in codoped SACs; histogram of $\Delta E(oxo)$ and $\Delta E(HAT)$ for all metal and oxidation state; comparison of $\Delta E(oxo)$ and $\Delta E(HAT)$ in Fe(II)/Fe(III) codoped SACs; statistics and histograms of $\Delta E(rebound)$ in codoped SACs; statistics and histograms of $\Delta E(release)$ in codoped SACs; Total energies for SAC intermediates of selected codoped SACs; comparison of $\Delta E(oxo)$ and $\Delta E(HAT)$ in Fe(II)/ Ru(II) codoped SACs; comparison of $\Delta E(oxo)$ and $\Delta E(HAT)$ between 2p and 3p coordination; $\Delta E(oxo)$ vs $\Delta E(HAT)$ reaction energies of codoped SACs in oxidation state III; linear fits and Pearson's r values of $\Delta E(oxo)$ vs $\Delta E(HAT)$ in codoped SACs; ($\Delta E(oxo) + \Delta E(HAT)$) value of optimal catalysts; total energies and spin splitting energies for LS and IS SACs; relative energetics of the catalytic cycle; thermal vs kinetics barrier of optima catalyst; Total DOS of selected codoped SACs relative energies of TDTS and TDI. (PDF)

Coordinates of structures from the codoped SACs dataset; coordinates of reference molecules; total electronic energies for codoped SACs dataset; reaction energies for each step in the codoped SACs dataset. (ZIP)

This material is available free of charge via the Internet at http://pubs.acs.org.

ACKNOWLEDGMENT

This research was funded by the National Science Foundation (grant number CBET-1846426) as well as a National Science Foundation Graduate Research Fellowship under Grant #1122374 (to A.N.). H.J.K. holds an Alfred P. Sloan Fellowship in Chemistry, which supported this work. This work was carried out in part using computational resources from the Extreme Science and Engineering Discovery Environment (XSEDE), which is supported by National Science Foundation grant number ACI-1548562. The authors thank Adam H. Steeves for providing a critical reading of the manuscript.

REFERENCES

- (1) Control methane to slow global warming fast. *Nature* **2021**, *596* (7873), 461-461. DOI: 10.1038/d41586-021-02287-y.
- (2) Tomkins, P.; Ranocchiari, M.; van Bokhoven, J. A. Direct Conversion of Methane to Methanol under Mild Conditions over Cu-Zeolites and beyond. *Accounts of Chemical Research* **2017**, *50* (2), 418-425. DOI: 10.1021/acs.accounts.6b00534.
- (3) Ravi, M.; Ranocchiari, M.; van Bokhoven, J. A. The Direct Catalytic Oxidation of Methane to Methanol-A Critical Assessment. *Angewandte Chemie-International Edition* **2017**, *56* (52), 16464-16483. DOI: 10.1002/anie.201702550.
- (4) Latimer, A. A.; Kakekhani, A.; Kulkarni, A. R.; Norskov, J. K. Direct Methane to Methanol: The Selectivity-Conversion Limit and Design Strategies. *Acs Catalysis* **2018**, *8* (8), 6894-6907. DOI: 10.1021/acscatal.8b00220.
- (5) Nandy, A.; Duan, C. R.; Goffinet, C.; Kulik, H. J. New Strategies for Direct Methane-to-Methanol Conversion from Active Learning Exploration of 16 Million Catalysts. *Jacs Au* **2022**, *2* (5), 1200-1213. DOI: 10.1021/jacsau.2c00176.
- (6) Price, J. C.; Barr, E. W.; Tirupati, B.; Bollinger, J. M.; Krebs, C. The first direct characterization of a high-valent iron intermediate in the reaction of an alpha-ketoglutarate-dependent dioxygenase: A high-spin Fe(IV) complex in taurine/alpha-ketoglutarate dioxygenase (TauD) from Escherichia coli. *Biochemistry* **2003**, *42* (24), 7497-7508. DOI: 10.1021/bi030011f.
- (7) Price, J. C.; Barr, E. W.; Glass, T. E.; Krebs, C.; Bollinger, J. M. Evidence for hydrogen abstraction from C1 of taurine by the high-spin Fe(IV) intermediate detected during oxygen activation by taurine :alpha-ketoglutarate dioxygenase (TauD). *Journal of the American Chemical Society* **2003**, *125* (43), 13008-13009. DOI: 10.1021/ja037400h.
- (8) Eichhorn, E.; vanderPloeg, J. R.; Kertesz, M. A.; Leisinger, T. Characterization of alphaketoglutarate-dependent taurine dioxygenase from Escherichia coli. *Journal of Biological Chemistry* **1997**, *272* (37), 23031-23036. DOI: 10.1074/jbc.272.37.23031.
- (9) Oloo, W. N.; Que, L. Bioinspired Nonheme Iron Catalysts for C-H and C=C Bond Oxidation: Insights into the Nature of the Metal-Based Oxidants. *Accounts of Chemical Research* **2015**, *48* (9), 2612-2621. DOI: 10.1021/acs.accounts.5b00053.
- (10) Biswas, A. N.; Puri, M.; Meier, K. K.; Oloo, W. N.; Rohde, G. T.; Bominaar, E. L.; Munck, E.; Que, L. Modeling TauD-J: A High-Spin Nonheme Oxoiron(IV) Complex with High Reactivity toward C-H Bonds. *Journal of the American Chemical Society* **2015**, *137* (7), 2428-2431. DOI: 10.1021/ja511757j.
- (11) Que, L.; Tolman, W. B. Biologically inspired oxidation catalysis. *Nature* **2008**, *455* (7211), 333-340. DOI: 10.1038/nature07371.
- (12) Periana, R. A.; Taube, D. J.; Gamble, S.; Taube, H.; Satoh, T.; Fujii, H. Platinum catalysts for the high-yield oxidation of methane to a methanol derivative. *Science* **1998**, *280* (5363), 560-564. DOI: 10.1126/science.280.5363.560.
- (13) Muehlhofer, M.; Strassner, T.; Herrmann, W. A. New catalyst systems for the catalytic conversion of methane into methanol. *Angewandte Chemie-International Edition* **2002**, *41* (10), 1745-+. DOI: 10.1002/1521-3773(20020517)41:10<1745::aid-anie1745>3.0.co;2-e.
- (14) Shilov, A. E.; Shul'pin, G. B. Activation of C-H bonds by metal complexes. *Chemical Reviews* **1997**, *97* (8), 2879-2932. DOI: 10.1021/cr9411886.
- (15) Jones, C. J.; Taube, D.; Ziatdinov, V. R.; Periana, R. A.; Nielsen, R. J.; Oxgaard, J.; Goddard, W. A. Selective oxidation of methane to methanol catalyzed, with C-H activation, by

- homogeneous, cationic gold. *Angewandte Chemie-International Edition* **2004**, *43* (35), 4626-4629. DOI: 10.1002/anie.200461055.
- (16) Lan, Z. Z.; Sharada, S. M. Linear free energy relationships for transition metal chemistry: case study of CH activation with copper-oxygen complexes. *Physical Chemistry Chemical Physics* **2020**, *22* (14), 7155-7159. DOI: 10.1039/d0cp01245a.
- (17) Lan, Z. Z.; Sharada, S. M. Computational strategies to probe CH activation in dioxodicopper complexes. *Physical Chemistry Chemical Physics* **2018**, *20* (40), 25602-25614. DOI: 10.1039/c8cp05096a.
- (18) Palkovits, R.; Antonietti, M.; Kuhn, P.; Thomas, A.; Schuth, F. Solid Catalysts for the Selective Low-Temperature Oxidation of Methane to Methanol. *Angewandte Chemie-International Edition* **2009**, *48* (37), 6909-6912. DOI: 10.1002/anie.200902009.
- (19) Dinh, K. T.; Sullivan, M. M.; Serna, P.; Meyer, R. J.; Dinca, M.; Roman-Leshkov, Y. Viewpoint on the Partial Oxidation of Methane to Methanol Using Cu- and Fe-Exchanged Zeolites. *Acs Catalysis* **2018**, *8* (9), 8306-8313. DOI: 10.1021/acscatal.8b01180.
- (20) Szecsenyi, A.; Li, G. N.; Gascon, J.; Pidko, E. A. Mechanistic Complexity of Methane Oxidation with H2O2 by Single-Site Fe/ZSM-5 Catalyst. *Acs Catalysis* **2018**, *8* (9), 7961-7972. DOI: 10.1021/acscatal.8b01672.
- (21) Qiao, B. T.; Wang, A. Q.; Yang, X. F.; Allard, L. F.; Jiang, Z.; Cui, Y. T.; Liu, J. Y.; Li, J.; Zhang, T. Single-atom catalysis of CO oxidation using Pt-1/FeOx. *Nature Chemistry* **2011**, *3* (8), 634-641. DOI: 10.1038/nchem.1095.
- (22) Yang, X. F.; Wang, A. Q.; Qiao, B. T.; Li, J.; Liu, J. Y.; Zhang, T. Single-Atom Catalysts: A New Frontier in Heterogeneous Catalysis. *Accounts of Chemical Research* **2013**, *46* (8), 1740-1748. DOI: 10.1021/ar300361m.
- (23) O'Connor, N. J.; Jonayat, A. S. M.; Janik, M. J.; Senftle, T. P. Interaction trends between single metal atoms and oxide supports identified with density functional theory and statistical learning. *Nature Catalysis* **2018**, *1* (7), 531-539. DOI: 10.1038/s41929-018-0094-5.
- (24) Peters, B.; Scott, S. L. Single atom catalysts on amorphous supports: A quenched disorder perspective. *Journal of Chemical Physics* **2015**, *142* (10), 104708. DOI: 10.1063/1.4914145.
- (25) Zhuo, H. Y.; Zhang, X.; Liang, J. X.; Yu, Q.; Xiao, H.; Li, J. Theoretical Understandings of Graphene-based Metal Single-Atom Catalysts: Stability and Catalytic Performance. *Chemical Reviews* **2020**, *120* (21), 12315-12341. DOI: 10.1021/acs.chemrev.0c00818.
- (26) Jiang, K.; Siahrostami, S.; Akey, A. J.; Li, Y. B.; Lu, Z. Y.; Lattimer, J.; Hu, Y. F.; Stokes, C.; Gangishetty, M.; Chen, G. X.; et al. Transition-Metal Single Atoms in a Graphene Shell as Active Centers for Highly Efficient Artificial Photosynthesis. *Chem* **2017**, *3* (6), 950-960. DOI: 10.1016/j.chempr.2017.09.014.
- (27) Jiang, K.; Siahrostami, S.; Zheng, T. T.; Hu, Y. F.; Hwang, S.; Stavitski, E.; Peng, Y. D.; Dynes, J.; Gangisetty, M.; Su, D.; et al. Isolated Ni single atoms in graphene nanosheets for high-performance CO2 reduction. *Energy & Environmental Science* **2018**, *11* (4), 893-903. DOI: 10.1039/c7ee03245e.
- (28) Jia, H. J.; Nandy, A.; Liu, M. J.; Kulik, H. J. Modeling the roles of rigidity and dopants in single-atom methane-to-methanol catalysts. *Journal of Materials Chemistry A* **2022**, *10* (11), 6193-6203. DOI: 10.1039/d1ta08502f.
- (29) Jiao, L.; Yan, H. Y.; Wu, Y.; Gu, W. L.; Zhu, C. Z.; Du, D.; Lin, Y. H. When Nanozymes Meet Single-Atom Catalysis. *Angewandte Chemie-International Edition* **2020**, *59* (7), 2565-2576. DOI: 10.1002/anie.201905645.

- (30) Kumar, P.; Al-Attas, T. A.; Hu, J. G.; Kibria, M. G. Single Atom Catalysts for Selective Methane Oxidation to Oxygenates. *Acs Nano* **2022**, *16* (6), 8557-8618. DOI: 10.1021/acsnano.2c02464.
- (31) Luo, L. H.; Luo, J.; Li, H. L.; Ren, F. N.; Zhang, Y. F.; Liu, A. D.; Li, W. X.; Zeng, J. Water enables mild oxidation of methane to methanol on gold single-atom catalysts. *Nature Communications* **2021**, *12* (1). DOI: 10.1038/s41467-021-21482-z.
- (32) Wang, S. M.; Xin, Y.; Yuan, J. Y.; Wang, L. B.; Zhang, W. H. Direct conversion of methane to methanol on boron nitride-supported copper single atoms. *Nanoscale* **2022**, *14* (14), 5447-5453. DOI: 10.1039/d1nr08466f.
- (33) Huang, E. R.; Liu, P. Theoretical Perspective of Promoting Direct Methane-to-Methanol Conversion at Complex Metal Oxide-Metal Interfaces. *Journal of Physical Chemistry Letters* **2023**, *14* (29), 6556-6563. DOI: 10.1021/acs.jpclett.3c01525.
- (34) Liu, F.; Yang, T. H.; Yang, J.; Xu, E.; Bajaj, A.; Kulik, H. J. Bridging the Homogeneous-Heterogeneous Divide: Modeling Spin for Reactivity in Single Atom Catalysis. *Frontiers in Chemistry* **2019**, *7*, 219. DOI: 10.3389/fchem.2019.00219.
- (35) Wang, A. Q.; Li, J.; Zhang, T. Heterogeneous single-atom catalysis. *Nature Reviews Chemistry* **2018**, *2* (6), 65-81. DOI: 10.1038/s41570-018-0010-1.
- (36) Chen, Y. J.; Ji, S. F.; Wang, Y. G.; Dong, J. C.; Chen, W. X.; Li, Z.; Shen, R. A.; Zheng, L. R.; Zhuang, Z. B.; Wang, D. S.; et al. Isolated Single Iron Atoms Anchored on N-Doped Porous Carbon as an Efficient Electrocatalyst for the Oxygen Reduction Reaction. *Angewandte Chemie-International Edition* **2017**, *56* (24), 6937-6941. DOI: 10.1002/anie.201702473.
- (37) Cheng, N. C.; Zhang, L.; Doyle-Davis, K.; Sun, X. L. Single-Atom Catalysts: From Design to Application. *Electrochemical Energy Reviews* **2019**, *2* (4), 539-573. DOI: 10.1007/s41918-019-00050-6.
- (38) Wei, Z. X.; Zhu, Y. T.; Liu, J. Y.; Zhang, Z. C.; Hu, W. P.; Xu, H.; Feng, Y. Z.; Ma, J. M. Recent advance in single-atom catalysis. *Rare Metals* **2021**, *40* (4), 767-789. DOI: 10.1007/s12598-020-01592-1.
- (39) Dzara, M. J.; Artyushkova, K.; Sougrati, M. T.; Ngo, C.; Fitzgerald, M. A.; Serov, A.; Zulevi, B.; Atanassov, P.; Jaouen, F.; Pylypenko, S. Characterizing Complex Gas-Solid Interfaces with in Situ Spectroscopy: Oxygen Adsorption Behavior on Fe-N-C Catalysts. *Journal of Physical Chemistry C* **2020**, *124* (30), 16529-16543. DOI: 10.1021/acs.jpcc.0c05244.
- (40) Liu, W. G.; Zhang, L. L.; Liu, X.; Liu, X. Y.; Yang, X. F.; Miao, S.; Wang, W. T.; Wang, A. Q.; Zhang, T. Discriminating Catalytically Active FeNx Species of Atomically Dispersed FeN-C Catalyst for Selective Oxidation of the C-H Bond. *Journal of the American Chemical Society* **2017**, *139* (31), 10790-10798. DOI: 10.1021/jacs.7b05130.
- (41) Ma, W.; Wan, H.; Zhang, L. L.; Zheng, J. Y.; Zhou, Z. Single-atom catalysts for electrochemical energy storage and conversion. *Journal of Energy Chemistry* **2021**, *63*, 170-194. DOI: 10.1016/j.jechem.2021.08.041.
- (42) Ma, W.; Deng, Z.; Zhang, X. J.; Zhang, Z.; Zhou, Z. Regulating the electronic structure of single-atom catalysts for electrochemical energy conversion. *Journal of Materials Chemistry A* **2023**, *11* (24), 12643-12658. DOI: 10.1039/d3ta00156c.
- (43) Liu, W. G.; Zhang, L. L.; Yan, W. S.; Liu, X. Y.; Yang, X. F.; Miao, S.; Wang, W. T.; Wang, A. Q.; Zhang, T. Single-atom dispersed Co-N-C catalyst: structure identification and performance for hydrogenative coupling of nitroarenes. *Chemical Science* **2016**, *7* (9), 5758-5764. DOI: 10.1039/c6sc02105k.

- (44) Zhang, C. H.; Yang, S. Z.; Wu, J. J.; Liu, M. J.; Yazdi, S.; Ren, M. Q.; Sha, J. W.; Zhong, J.; Nie, K. Q.; Jalilov, A. S.; et al. Electrochemical CO2 Reduction with Atomic Iron-Dispersed on Nitrogen-Doped Graphene. *Advanced Energy Materials* **2018**, *8* (19). DOI: 10.1002/aenm.201703487.
- (45) Deng, D. H.; Chen, X. Q.; Yu, L.; Wu, X.; Liu, Q. F.; Liu, Y.; Yang, H. X.; Tian, H. F.; Hu, Y. F.; Du, P. P.; et al. A single iron site confined in a graphene matrix for the catalytic oxidation of benzene at room temperature. *Science Advances* **2015**, *1* (11). DOI: 10.1126/sciadv.1500462. (46) Kramm, U. I.; Abs-Wurmbach, I.; Herrmann-Geppert, I.; Radnik, J.; Fiechter, S.; Bogdanoff, P. Influence of the Electron-Density of FeN4-Centers Towards the Catalytic Activity of Pyrolyzed FeTMPPCl-Based ORR-Electrocatalysts. *Journal of the Electrochemical Society* **2011**, *158* (1), B69-B78. DOI: 10.1149/1.3499621.
- (47) Marshall-Roth, T.; Libretto, N. J.; Wrobel, A. T.; Anderton, K. J.; Pegis, M. L.; Ricke, N. D.; Voorhis, T. V.; Miller, J. T.; Surendranath, Y. A pyridinic Fe-N4 macrocycle models the active sites in Fe/N-doped carbon electrocatalysts. *Nature communications* **2020**, *11* (1), 5283. (48) Zitolo, A.; Goellner, V.; Armel, V.; Sougrati, M. T.; Mineva, T.; Stievano, L.; Fonda, E.;
- (48) Zitolo, A.; Goellner, V.; Armel, V.; Sougrati, M. T.; Mineva, T.; Stievano, L.; Fonda, E. Jaouen, F. Identification of catalytic sites for oxygen reduction in iron- and nitrogen-doped graphene materials. *Nature Materials* **2015**, *14* (9), 937-+. DOI: 10.1038/nmat4367.
- (49) Zhang, J. Q.; Zhao, Y. F.; Chen, C.; Huang, Y. C.; Dong, C. L.; Chen, C. J.; Liu, R. S.; Wang, C. Y.; Yan, K.; Li, Y. D.; et al. Tuning the Coordination Environment in Single-Atom Catalysts to Achieve Highly Efficient Oxygen Reduction Reactions. *Journal of the American Chemical Society* **2019**, *141* (51), 20118-20126. DOI: 10.1021/jacs.9b09352.
- (50) Li, J. J.; Zhang, Y. M.; Zhang, X. H.; Huang, J. Z.; Han, J. C.; Zhang, Z. H.; Han, X. J.; Xu, P.; Song, B. S, N Dual-Doped Graphene-like Carbon Nanosheets as Efficient Oxygen Reduction Reaction Electrocatalysts. *Acs Applied Materials & Interfaces* **2017**, *9* (1), 398-405. DOI: 10.1021/acsami.6b12547.
- (51) Li, X. H.; Yang, X. X.; Liu, L. T.; Zhao, H.; Li, Y. W.; Zhu, H. Y.; Chen, Y. Z.; Guo, S. W.; Liu, Y. N.; Tan, Q.; et al. Chemical Vapor Deposition for N/S-Doped Single Fe Site Catalysts for the Oxygen Reduction in Direct Methanol Fuel Cells. *Acs Catalysis* **2021**, *11* (12), 7450-7459. DOI: 10.1021/acscatal.0c05446.
- (52) Yuan, K.; Lutzenkirchen-Hecht, D.; Li, L. B.; Shuai, L.; Li, Y. Z.; Cao, R.; Qiu, M.; Zhuang, X. D.; Leung, M. K. H.; Chen, Y. W.; et al. Boosting Oxygen Reduction of Single Iron Active Sites via Geometric and Electronic Engineering: Nitrogen and Phosphorus Dual Coordination. *Journal of the American Chemical Society* **2020**, *142* (5), 2404-2412. DOI: 10.1021/jacs.9b11852.
- (53) Shang, H. S.; Zhou, X. Y.; Dong, J. C.; Li, A.; Zhao, X.; Liu, Q. H.; Lin, Y.; Pei, J. J.; Li, Z.; Jiang, Z. L.; et al. Engineering unsymmetrically coordinated Cu-S1N3 single atom sites with enhanced oxygen reduction activity. *Nature Communications* **2020**, *11* (1). DOI: 10.1038/s41467-020-16848-8.
- (54) Fei, H. L.; Dong, J. C.; Arellano-Jimenez, M. J.; Ye, G. L.; Kim, N. D.; Samuel, E. L. G.; Peng, Z. W.; Zhu, Z.; Qin, F.; Bao, J. M.; et al. Atomic cobalt on nitrogen-doped graphene for hydrogen generation. *Nature Communications* **2015**, *6*, 8668. DOI: 10.1038/ncomms9668. (55) Wang, A.; Zhang, T. Water splitting: Taking cobalt in isolation. *Nature Energy* **2016**, *1*, 15019.
- (56) Nandy, A.; Kulik, H. J. Why Conventional Design Rules for C-H Activation Fail for Open-Shell Transition-Metal Catalysts. *Acs Catalysis* **2020**, *10* (24), 15033-15047. DOI: 10.1021/acscatal.0c04300.

- (57) Jiao, L.; Xu, W. Q.; Zhang, Y.; Wu, Y.; Gu, W. L.; Ge, X. X.; Chen, B. B.; Zhu, C. Z.; Guo, S. J. Boron-doped Fe-N-C single-atom nanozymes specifically boost peroxidase-like activity. *Nano Today* **2020**, *35*. DOI: 10.1016/j.nantod.2020.100971.
- (58) Mineva, T.; Matanovic, I.; Atanassov, P.; Sougrati, M. T.; Stievano, L.; Clemancey, M.; Kochem, A.; Latour, J. M.; Jaouen, F. Understanding Active Sites in Pyrolyzed Fe-N-C Catalysts for Fuel Cell Cathodes by Bridging Density Functional Theory Calculations and Fe-57 Mossbauer Spectroscopy. *Acs Catalysis* **2019**, *9* (10), 9359-9371. DOI: 10.1021/acscatal.9b02586.
- (59) Xu, H. X.; Cheng, D. J.; Cao, D. P.; Zeng, X. C. A universal principle for a rational design of single-atom electrocatalysts (vol 1, pg 339, 2018). *Nature Catalysis* **2018**, *I* (8), 632-632. DOI: 10.1038/s41929-018-0127-0.
- (60) Fung, V.; Hu, G. X.; Wu, Z. L.; Jiang, D. E. Descriptors for Hydrogen Evolution on Single Atom Catalysts in Nitrogen-Doped Graphene. *Journal of Physical Chemistry C* **2020**, *124* (36), 19571-19578. DOI: 10.1021/acs.jpcc.0c04432.
- (61) Xi, Y. J.; Heyden, A. Direct Oxidation of Methane to Methanol Enabled by Electronic Atomic Monolayer-Metal Support Interaction. *Acs Catalysis* **2019**, *9* (7), 6073-6079. DOI: 10.1021/acscatal.9b01619.
- (62) Hong, S.; Mpourmpakis, G. Mechanistic understanding of methane-to-methanol conversion on graphene-stabilized single-atom iron centers. *Catalysis Science & Technology* **2021**, *11* (19), 6390-6400. DOI: 10.1039/d1cy00826a.
- (63) Zhang, L. Z.; Jia, Y.; Gao, G. P.; Yan, X. C.; Chen, N.; Chen, J.; Soo, M. T.; Wood, B.; Yang, D. J.; Du, A. J.; et al. Graphene Defects Trap Atomic Ni Species for Hydrogen and Oxygen Evolution Reactions. *Chem* **2018**, *4* (2), 285-297. DOI: 10.1016/j.chempr.2017.12.005.
- (64) Gao, Y.; Cai, Z. W.; Wu, X. C.; Lv, Z. L.; Wu, P.; Cai, C. X. Graphdiyne-Supported Single-Atom-Sized Fe Catalysts for the Oxygen Reduction Reaction: DFT Predictions and Experimental Validations. *Acs Catalysis* **2018**, *8* (11), 10364-10374. DOI: 10.1021/acscatal.8b02360.
- (65) Kraushofer, F.; Parkinson, G. S. Single-Atom Catalysis: Insights from Model Systems. *Chemical Reviews* **2022**, *122* (18), 14911-14939. DOI: 10.1021/acs.chemrev.2c00259.
- (66) Patniboon, T.; Hansen, H. A. Acid-Stable and Active M-N-C Catalysts for the Oxygen Reduction Reaction: The Role of Local Structure. *Acs Catalysis* **2021**, *11* (21), 13102-13118. DOI: 10.1021/acscatal.1c02941.
- (67) Tan, X.; Tahini, H. A.; Smith, S. C. Defect Engineering in Graphene-Confined Single-Atom Iron Catalysts for Room-Temperature Methane Conversion. *Journal of Physical Chemistry C* **2021**, *125* (23), 12628-12635. DOI: 10.1021/acs.jpcc.1c01806.
- (68) Goldsmith, B. R.; Sanderson, E. D.; Bean, D.; Peters, B. Isolated catalyst sites on amorphous supports: A systematic algorithm for understanding heterogeneities in structure and reactivity. *Journal of Chemical Physics* **2013**, *138* (20). DOI: 10.1063/1.4807384.
- (69) Sperger, T.; Sanhueza, I. A.; Schoenebeck, F. Computation and Experiment: A Powerful Combination to Understand and Predict Reactivities. *Accounts of Chemical Research* **2016**, *49* (6), 1311-1319. DOI: 10.1021/acs.accounts.6b00068.
- (70) Latimer, A. A.; Kulkarni, A. R.; Aljama, H.; Montoya, J. H.; Yoo, J. S.; Tsai, C.; Abild-Pedersen, F.; Studt, F.; Norskov, J. K. Understanding trends in C-H bond activation in heterogeneous catalysis. *Nature Materials* **2017**, *16* (2), 225-229. DOI: 10.1038/nmat4760.
- (71) Medford, A. J.; Vojvodic, A.; Hummelshoj, J. S.; Voss, J.; Abild-Pedersen, F.; Studt, F.; Bligaard, T.; Nilsson, A.; Norskov, J. K. From the Sabatier principle to a predictive theory of

- transition-metal heterogeneous catalysis. *Journal of Catalysis* **2015**, *328*, 36-42. DOI: 10.1016/j.jcat.2014.12.033.
- (72) Abild-Pedersen, F.; Greeley, J.; Studt, F.; Rossmeisl, J.; Munter, T. R.; Moses, P. G.; Skulason, E.; Bligaard, T.; Norskov, J. K. Scaling properties of adsorption energies for hydrogen-containing molecules on transition-metal surfaces. *Physical Review Letters* **2007**, *99* (1). DOI: 10.1103/PhysRevLett.99.016105.
- (73) Bligaard, T.; Norskov, J. K.; Dahl, S.; Matthiesen, J.; Christensen, C. H.; Sehested, J. The Bronsted-Evans-Polanyi relation and the volcano curve in heterogeneous catalysis. *Journal of Catalysis* **2004**, *224* (1), 206-217. DOI: 10.1016/j.jcat.2004.02.034.
- (74) Ren, C. J.; Jiang, Q. Y.; Lin, W.; Zhang, Y. F.; Huang, S. P.; Ding, K. N. Density Functional Theory Study of Single-Atom V, Nb, and Ta Catalysts on Graphene and Carbon Nitride for Selective Nitrogen Reduction. *Acs Applied Nano Materials* **2020**, *3* (6), 5149-5159. DOI: 10.1021/acsanm.0c00512.
- (75) Nandy, A.; Zhu, J. Z.; Janet, J. P.; Duan, C. R.; Getman, R. B.; Kulik, H. J. Machine Learning Accelerates the Discovery of Design Rules and Exceptions in Stable Metal-Oxo Intermediate Formation. *Acs Catalysis* **2019**, *9* (9), 8243-8255. DOI: 10.1021/acscatal.9b02165. (76) Vennelakanti, V.; Nandy, A.; Kulik, H. J. The Effect of Hartree-Fock Exchange on Scaling Relations and Reaction Energetics for C-H Activation Catalysts. *Topics in Catalysis* **2022**, *65* (1-4), 296-311. DOI: 10.1007/s11244-021-01482-5.
- (77) Gomez-Bombarelli, R.; Aguilera-Iparraguirre, J.; Hirzel, T. D.; Duvenaud, D.; Maclaurin, D.; Blood-Forsythe, M. A.; Chae, H. S.; Einzinger, M.; Ha, D. G.; Wu, T.; et al. Design of efficient molecular organic light-emitting diodes by a high-throughput virtual screening and experimental approach. *Nature Materials* **2016**, *15* (10), 1120-+. DOI: 10.1038/nmat4717. (78) Curtarolo, S.; Hart, G. L. W.; Nardelli, M. B.; Mingo, N.; Sanvito, S.; Levy, O. The high-throughput highway to computational materials design. *Nature Materials* **2013**, *12* (3), 191-201. DOI: 10.1038/nmat3568.
- (79) Foscato, M.; Jensen, V. R. Automated in Silico Design of Homogeneous Catalysts. *Acs Catalysis* **2020**, *10* (3), 2354-2377. DOI: 10.1021/acscatal.9b04952.
- (80) Zhao, K. Y.; Shen, Q. K.; Tao, Y.; Li, J. R.; Wang, M. L.; Li, C.; Xu, B. J. Atomically Dispersed N/O-Coordinated Cobalt Catalyst Enables Aerobic Oxygenation of Olefins under Ambient Conditions. *Acs Catalysis* **2023**, *13* (19), 12591-12600. DOI: 10.1021/acscatal.3c03209.
- (81) Sun, H.; Wang, M. F.; Du, X. C.; Jiao, Y.; Liu, S. S.; Qian, T.; Yan, Y. C.; Liu, C.; Liao, M.; Zhang, Q. H.; et al. Modulating the d-band center of boron doped single-atom sites to boost the oxygen reduction reaction. *Journal of Materials Chemistry A* **2019**, 7 (36), 20952-20957. DOI: 10.1039/c9ta06949f.
- (82) Groves, J. T.; McClusky, G. A. ALIPHATIC HYDROXYLATION VIA OXYGEN REBOUND OXYGEN-TRANSFER CATALYZED BY IRON. *Journal of the American Chemical Society* **1976**, *98* (3), 859-861. DOI: 10.1021/ja00419a049.
- (83) Xiao, D. J.; Bloch, E. D.; Mason, J. A.; Queen, W. L.; Hudson, M. R.; Planas, N.; Borycz, J.; Dzubak, A. L.; Verma, P.; Lee, K.; et al. Oxidation of ethane to ethanol by N2O in a metalorganic framework with coordinatively unsaturated iron(II) sites. *Nature Chemistry* **2014**, *6* (7), 590-595. DOI: 10.1038/nchem.1956.
- (84) Barona, M.; Ahn, S.; Morris, W.; Hoover, W.; Notestein, J. M.; Farha, O. K.; Snurr, R. Q. Computational Predictions and Experimental Validation of Alkane Oxidative Dehydrogenation by Fe2M MOF Nodes. *Acs Catalysis* **2020**, *10* (2), 1460-1469. DOI: 10.1021/acscatal.9b03932.

- (85) Ufimtsev, I. S.; Martinez, T. J. Quantum Chemistry on Graphical Processing Units. 3. Analytical Energy Gradients, Geometry Optimization, and First Principles Molecular Dynamics. *Journal of Chemical Theory and Computation* **2009**, *5* (10), 2619-2628. DOI: 10.1021/ct9003004.
- (86) Rohrdanz, M. A.; Martins, K. M.; Herbert, J. M. A long-range-corrected density functional that performs well for both ground-state properties and time-dependent density functional theory excitation energies, including charge-transfer excited states. *Journal of Chemical Physics* **2009**, *130* (5). DOI: 10.1063/1.3073302.
- (87) Kulik, H. J.; Zhang, J. Y.; Klinman, J. P.; Martinez, T. J. How Large Should the QM Region Be in QM/MM Calculations? The Case of Catechol O-Methyltransferase. *Journal of Physical Chemistry B* **2016**, *120* (44), 11381-11394. DOI: 10.1021/acs.jpcb.6b07814.
- (88) Isborn, C. M.; Luehr, N.; Ufimtsev, I. S.; Martinez, T. J. Excited-State Electronic Structure with Configuration Interaction Singles and Tamm-Dancoff Time-Dependent Density Functional Theory on Graphical Processing Units. *Journal of Chemical Theory and Computation* **2011**, *7* (6), 1814-1823. DOI: 10.1021/ct200030k.
- (89) Hay, P. J.; Wadt, W. R. ABINITIO EFFECTIVE CORE POTENTIALS FOR MOLECULAR CALCULATIONS POTENTIALS FOR THE TRANSITION-METAL ATOMS SC TO HG. *Journal of Chemical Physics* **1985**, *82* (1), 270-283. DOI: 10.1063/1.448799.
- (90) Wadt, W. R.; Hay, P. J. ABINITIO EFFECTIVE CORE POTENTIALS FOR MOLECULAR CALCULATIONS POTENTIALS FOR MAIN GROUP ELEMENTS NA TO BI. *Journal of Chemical Physics* **1985**, *82* (1), 284-298. DOI: 10.1063/1.448800.
- (91) Saunders, V. R.; Hillier, I. H. LEVEL-SHIFTING METHOD FOR CONVERGING CLOSED SHELL HARTREE-FOCK WAVE-FUNCTIONS. *International Journal of Quantum Chemistry* **1973**, *7* (4), 699-705. DOI: 10.1002/qua.560070407.
- (92) Wang, L. P.; Song, C. C. Geometry optimization made simple with translation and rotation coordinates. *Journal of Chemical Physics* **2016**, *144* (21). DOI: 10.1063/1.4952956.
- (93) Ioannidis, E. I.; Gani, T. Z. H.; Kulik, H. J. molSimplify: A toolkit for automating discovery in inorganic chemistry. *Journal of Computational Chemistry* **2016**, *37* (22), 2106-2117. DOI: 10.1002/jcc.24437.
- (94) O'Boyle, N. M.; Banck, M.; James, C. A.; Morley, C.; Vandermeersch, T.; Hutchison, G. R. Open Babel: An open chemical toolbox. *Journal of Cheminformatics* **2011**, *3*. DOI: 10.1186/1758-2946-3-33.
- (95) Nandy, A.; Duan, C. R.; Janet, J. P.; Gugler, S.; Kulik, H. J. Strategies and Software for Machine Learning Accelerated Discovery in Transition Metal Chemistry. *Industrial & Engineering Chemistry Research* **2018**, *57* (42), 13973-13986. DOI: 10.1021/acs.iecr.8b04015.
- (96) Neese, F. Software update: The ORCA program system-Version 5.0. *Wiley Interdisciplinary Reviews-Computational Molecular Science* **2022**, *12* (5). DOI: 10.1002/wcms.1606.
- (97) Larson, V. A.; Battistella, B.; Ray, K.; Lehnert, N.; Nam, W. Iron and manganese oxo complexes, oxo wall and beyond. *Nature Reviews Chemistry* **2020**, *4* (8), 404-419. DOI: 10.1038/s41570-020-0197-9.
- (98) Cao, L. L.; Luo, Q. Q.; Chen, J. J.; Wang, L.; Lin, Y.; Wang, H. J.; Liu, X. K.; Shen, X. Y.; Zhang, W.; Liu, W.; et al. Dynamic oxygen adsorption on single-atomic Ruthenium catalyst with high performance for acidic oxygen evolution reaction. *Nature Communications* **2019**, *10*. DOI: 10.1038/s41467-019-12886-z.

- (99) Harper, D. R.; Kulik, H. J. Computational Scaling Relationships Predict Experimental Activity and Rate-Limiting Behavior in Homogeneous Water Oxidation. *Inorganic Chemistry* **2022**, *61* (4), 2186-2197. DOI: 10.1021/acs.inorgchem.1c03376.
- (100) Jalama, K. Carbon dioxide hydrogenation over nickel-, ruthenium-, and copper-based catalysts: Review of kinetics and mechanism. *Catalysis Reviews-Science and Engineering* **2017**, *59* (2), 95-164. DOI: 10.1080/01614940.2017.1316172.
- (101) Ayers, P. W. An elementary derivation of the hard/soft-acid/base principle. *Journal of Chemical Physics* **2005**, *122* (14). DOI: 10.1063/1.1897374.
- (102) Ayers, P. W.; Parr, R. G.; Pearson, R. G. Elucidating the hard/soft acid/base principle: A perspective based on half-reactions. *Journal of Chemical Physics* **2006**, *124* (19). DOI: 10.1063/1.2196882.
- (103) Gani, T. Z. H.; Kulik, H. J. Understanding and Breaking Scaling Relations in Single-Site Catalysis: Methane to Methanol Conversion by Fe-IV=O. *Acs Catalysis* **2018**, *8* (2), 975-986. DOI: 10.1021/acscatal.7b03597.
- (104) Rosen, A. S.; Notestein, J. M.; Snurr, R. Q. Structure-Activity Relationships That Identify Metal-Organic Framework Catalysts for Methane Activation. *Acs Catalysis* **2019**, *9* (4), 3576-3587. DOI: 10.1021/acscatal.8b05178.
- (105) van Santen, R. A.; Neurock, M.; Shetty, S. G. Reactivity Theory of Transition-Metal Surfaces: A Bronsted-Evans-Polanyi Linear Activation Energy-Free-Energy Analysis. *Chemical Reviews* **2010**, *110* (4), 2005-2048. DOI: 10.1021/cr9001808.
- (106) Simons, M. C.; Vitillo, J. G.; Babucci, M.; Hoffman, A. S.; Boubnov, A.; Beauvais, M. L.; Chen, Z. H. Y.; Cramer, C. J.; Chapman, K. W.; Bare, S. R.; et al. Structure, Dynamics, and Reactivity for Light Alkane Oxidation of Fe(II) Sites Situated in the Nodes of a Metal-Organic Framework. *Journal of the American Chemical Society* **2019**, *141* (45), 18142-18151. DOI: 10.1021/jacs.9b08686.
- (107) Vitillo, J. G.; Bhan, A.; Cramer, C. J.; Lu, C. C.; Gagliardi, L. Quantum Chemical Characterization of Structural Single Fe(II) Sites in MIL-Type Metal-Organic Frameworks for the Oxidation of Methane to Methanol and Ethane to Ethanol. *Acs Catalysis* **2019**, *9* (4), 2870-2879. DOI: 10.1021/acscatal.8b04813.

TOC Graphic

